GEOHORIZONS

Chronologic modeling of faulted and fractured reservoirs using geomechanically based restoration: Technique and industry applications

Laurent Maerten and Frantz Maerten

ABSTRACT

We have developed a geomechanically based restoration method to model reservoir deformation. The approach, founded on the finite-element method, simulates the physical behavior of the rock mass and considers heterogeneous material properties, bedding slip, and the mechanical interaction of faults. To demonstrate the method's potential, we analyze the deformation and fault growth in the hanging wall of a synsedimentary listric normal fault from a sand-box model, which provides an analog for evaluating complex faulted reservoirs. The numerical model results are then analyzed to investigate the chronology of faulting. The numerical model corresponds well to the physical model and provides additional insights about reservoir evolution and deformation. The approach is also tested on a natural example of folding using outcrop data to study contractional deformation.

These examples illustrate how undetected faults and fractures, reservoir compartmentalization, hydrocarbon-migration pathways, and hydrocarbon traps can be understood in the context of tectonic processes and how this understanding can be exploited in decision making and reducing risk. We conclude that the geomechanically based restoration of faulted and fractured reservoirs has significant potential for industry applications compared to common geometric restoration techniques, which lack a mechanical basis.

Manuscript received July 26, 2005; provisional acceptance October 18, 2005; revised manuscript received February 15, 2006; final acceptance February 24, 2006.
DOI:10.1306/02240605116

AUTHORS

LAURENT MAERTEN ~ *IGEOSS sarl, Cap Omega, Rond Point Benjamin Franklin, CS39521, 34960 Montpellier Cedex 2, France; laurent.maerten@igeoss.com*

Laurent received his M.Sc. degree in geology from the University of Montpellier, France, in 1994. He has completed his Ph.D. in geology and environmental sciences in 1999 at Stanford University in collaboration with Norsk Hydro. He worked at the French Petroleum Institute in Paris as a research engineer in structural geology for 2 years. Laurent is currently the chief executive officer and principal consultant of IGEOSS. His interests focus on geological structures, geomechanical modeling, three-dimensional restoration, and the development of innovative methods to improve hydrocarbon production in fractured reservoirs.

FRANTZ MAERTEN ~ *IGEOSS sarl, Cap Omega, Rond Point Benjamin Franklin, CS39521, 34960 Montpellier Cedex 2, France; frantz.maerten@igeoss.com*

Frantz has a bachelor's degree in physics and a master's degree in earth sciences from the University of Montpellier, France. He is also a Ph.D. candidate in both earth sciences and computer sciences in collaboration with Stanford University. Frantz was a computer engineer and research associate for 4 years in the Structural Geology and Geomechanics Group of Stanford University. He has developed and improved the numerical computer code Poly3D, and he is the principal inventor of Dynel and its technology. Frantz is the research and development director of IGEOSS. His interests focus on developing innovative numerical codes for modeling three-dimensional geological structures.

ACKNOWLEDGEMENTS

We are grateful to David Pollard for his encouragement and review, Ken McClay for his agreement to use one of his figures, and Loïc Bazalgette for providing the data of the Coulazou's fold. We thank the Structural Geology and Geomechanics Team of Stanford University as well as the IGEOSS' development team for their hard work. We also thank ChevronTexaco, ConocoPhillips, ExxonMobile, Repsol YPF, Shell, and Total for supporting and funding the project through a research and development consortium.

INTRODUCTION

Whether faults and fractures act as seals or conduits, and whether they are resolvable on seismic reflection surveys, they can significantly affect hydrocarbon migration and trap location, as well as flow of hydrocarbons to wells during production. Therefore, understanding the evolution of faults and fractures and physical properties through time should improve reservoir-simulation models and, in turn, significantly improve decision making and reduce production risks.

Structural heterogeneities, such as faults and fractures, are known to be capable of significantly altering the flow of hydrocarbons, either during the migration from the source to the reservoir rock or during production of the reservoir. Therefore, understanding and quantifying the spatial and temporal development of these features, as well as their properties (e.g., geometry, throw, aperture, permeability, etc.), can have great economical impact on the recovery of natural reserves. However, despite the tremendous detail now available from three-dimensional (3-D) seismic reflection techniques (Dorn, 1998), many of these features cannot be detected at the current resolution of the seismic reflection data, typically about 20–30 m (66–98 ft) of throw for faults in North Sea reservoirs. Furthermore, whereas these geophysical techniques adequately image the major geological structures, this only provides the present-day structural geometry of the subsurface, which commonly has resulted from multiple tectonic events, thereby increasing the complexity of the analysis. To more realistically model the spatial and temporal development of structural heterogeneities and to address these economical issues, a variety of numerical techniques have been developed. They fall into three main categories: (1) the geometric and kinematic approaches; (2) the stochastic approaches; and (3) the physical and geomechanical approaches.

The first category includes most of the restoration techniques used by structural geologists to check the consistency of the subsurface structural interpretations. Measures of gaps and overlaps between the restored parts of a model give qualitative values to check the strength of the geological interpretation. The geometrical methods proposed to restore geological structures are based on a variety of algorithms, which aim at reproducing natural deformation. For instance, the methods include balancing cross sections by flexural slip (Dahlstrom, 1969; Hossack, 1979; Davison, 1986) to model deformation accommodated by slip along an infinite number of bedding interfaces. Vertical (Gibbs, 1983; Williams and Vann, 1987) or inclined shear (White et al., 1986; Dula, 1991) techniques have been developed to simulate deformation accommodated by slip along an infinite number of vertical or inclined parallel faults, respectively. Geometrical (Gratier et al., 1991; Samson, 1996; Williams et al., 1997) unfolding methods for 3-D surfaces have been proposed, based on flexural slip and homogeneous inclined shear (Kerr et al., 1993; Griffiths et al., 2002). More simply, map-view restoration has been done using rigid translation and rotation of fault blocks (Dokka and Travis, 1990; Rouby et al., 1993) to model larger scale deformation. An analytical approach for 3-D surface unfolding has been proposed, based on surface parameterization and global deformation minimization (Lévy, 2000). These methods are based on geometrical assumptions (Rouby et al., 2000), such as preservation of area, minimization of deformation, minimization of changes in segment length, or minimization of shearing, constant fault slip, fixed faults in space, or discontinuous rigid blocks.

Lately, the use of these techniques has been extended to predict areas that have undergone large strains at subseismic reservoir scales and to relate the strains to structural heterogeneities such as faults and fractures (Hennings et al., 2000; Sanders et al., 2002, 2004). Although they have the attractiveness of modeling the kinematic evolution of deformed sedimentary basins back in time, these methods are not appropriate to compute fault-block deformation and fault-slip distributions, which are necessary to model both the fault development and the subseismic fractures. Natural deformation is a physical phenomenon that involves parameters such as the initial geometry, the distribution of mass, rock mechanical properties, and the forces that cause the deformation. Therefore, it is uncertain which geometric restoration algorithm should be used to model rock deformation (Hauge and Gray, 1996; Bulnes and McClay, 1999). Furthermore, these techniques are not based on the fundamental principles of the conservation of mass and momentum, which govern rock deformation. Consequently, no rock mechanical properties can be incorporated in the model, no stress boundary condition can be applied to simulate tectonic loading, and no mechanical interaction among the faults is considered. In addition, only strain, which is strongly dependent on the geometric restoration algorithm used, is calculated (Erickson et al., 2000; Hennings et al., 2000; Rouby et al., 2000; Sanders et al., 2004), whereas fracture mechanics tell us that the state of stress is required to explain how fractures develop and interact.

Stochastic techniques are commonly based on the fracture power-law size distribution, calibrated using field or seismic data (Childs et al., 1990; Walsh and Watterson, 1991; Schlische et al., 1996). For instance, the fractal model for faulting is used to predict the number of subseismic faults by extrapolation of the power laws (Sassi et al., 1992; Yielding et al., 1992; Gauthier and Lake, 1993; Gillespie et al., 1993). Although the size distributions are predictable, these techniques pay little or no consideration to physical concepts that govern fault development. Consequently, they cannot take advantage of the constraints imposed by physical laws to predict the orientations and the location of these geological features.

Recent studies (Maerten, 1999; Bourne et al., 2000; Maerten et al., in press) have shown that adding a geomechanical rationale to stochastic techniques improves their predictive capability and leads to more realistic faulted and fractured reservoir models. (A finite-element approach [FEM] for 3-D surface unfolding has been proposed based on strain minimization; Dunbar and Cook, 2003.) These techniques fall into the third category. As opposed to the geometric approach, the geomechanical approach considers mechanical concepts and the fundamental physical laws that govern fracture and fault development. The basic methodology consists of calculating the stress distribution at the time of fracturing using the available reservoir structure data, such as faults, fractures and folds, and rock properties and the tectonic setting that can be characterized by stress or strain magnitude and orientation. Then, the calculated stress fields, perturbed by the main structures, combined with rock failure criteria, are used to model fracture networks (i.e., orientation, location, and spatial density). Applications to both outcrops (Kattenhorn et al., 2000; Bourne and Willemse, 2001; Bai et al., 2002; Guiton et al., 2003b; Healy et al., 2004, Davatzes et al., 2005) and reservoirs (Maerten, 1999; Bourne et al., 2000; Guiton, 2001; Maerten et al., 2002, in press) demonstrate how geomechanics can provide a high degree of predictability of natural fracture and fault networks. The 3-D boundary element method has been successfully applied to model subseismic faults (Maerten, 1999; Maerten et al., in press) in the northern North Sea's highly faulted reservoirs as well as undetected fractures in naturally fractured carbonate reservoirs (Bourne et al., 2000). Three-dimensional FEM has been recently developed to forward model diffuse fracture networks in folded sedimentary layers (Guiton et al., 2003a) and applied to a Middle East folded hydrocarbon reservoir (Guiton, 2001). However, whereas numerical models of rock deformation based on continuum mechanics provide an important tool for characterizing geologic structures in the context of hydrocarbon exploration and production, they do not effectively model past fracture development because of their geometric dependence on the available present-day subsurface structural model of the reservoir to infer stress distribution.

In this contribution, we propose a new numerical method developed by L. Maerten and F. Maerten (2001, unpublished data) that combines the restoration of geological structures with geomechanics. This technique allows computing geologic deformation and perturbed stresses through time for key geologic settings and tectonic episodes. The method, based on the FEM, simulates the geomechanical behavior of complex geological structures such as folded and faulted rock. It honors the full complement of physical laws that govern geological deformation, including conservation of momentum, mass, and energy. Therefore, physical laws and linear elastic theory replace kinematic and geometric constraints used by the existing methods for the restoration of geological structures.

We apply the two-dimensional (2-D) FEM to analyze deformation and fault growth in the hanging wall of a synsedimentary listric normal fault from a sand-box experiment (McClay, 1990). The physical model constitutes a good-quality analog for evaluating complex faulted and fractured reservoirs. It provides good controls on both the interpretation of the observed structures and the analysis of their development through time. The restoration methodology is described, and we explain how fault chronology can be inferred and how undetected faults can be modeled. We also show how this technique applies to a natural example of contractional structures and how it can help petroleum engineers to define reservoir compartmentalization, hydrocarbon-migration pathways, and trap geometries, with the goals of reducing production risks and improving the decision-making process.

PRINCIPLES AND METHOD

The geomechanically based restorations described in this study were performed with Dynel, a 2-D and 3-D geomechanical computer program that has been developed to model complex geological structures with a variety of boundary conditions or constraints. In this study, we only consider the 2-D formulation to restore geological cross sections.

Principles

Dynel is a continuum code based on FEM (Hughes, 1987) for modeling the behavior of complex geological structures, such as folded, fractured, and faulted rock. Its formulation can accommodate large displacements and strains for a heterogeneous, anisotropic, and discontinuous medium. Stresses that would exceed the elastic limit, and thereby subject the model to nonrecoverable deformation, are not considered (Novozhilov, 1953).

Models are discretized with linear triangular elements in 2-D, which form a mesh that is adjusted by the user to fit the shape of the structures under consideration. Each element has assigned material properties that may differ from element to element, and each behaves according to a prescribed linear elastic law in response to constraints such as applied and/or internal forces, displacements, and interface contact reactions. As opposed to the standard implicit FEM (Hughes, 1987), where a global stiffness matrix is built for solving for the unknown displacements, we use an iterative solver based on the Gauss-Seidel method (Golub and Van Loan, 1996). This solver allows forces to be transmitted from node to node through the entire system until equilibrium is obtained. Nodal forces are computed using the stress state of each connected element and consider other forces such as external and contact forces.

This explicit formulation of the FEM used here makes it ideally suited for modeling complex geological and geomechanical problems that consist of several stages, such as restoration, sedimentation, and erosion. Furthermore, this formulation results in much less memory allocation, and computation can easily be distributed among computers in a cluster. The explicit solution scheme also gives a stable solution to unstable numerical processes. It permits one to develop new complex constraints, such as unfolding on nonplanar surfaces, contact interaction, and mixing of different boundary conditions (i.e., displacement and stress [traction] boundary conditions).

Methods

Determination of the Element and Nodal Deformation

Initially, the system is at rest in equilibrium ($\Sigma F = 0$). Applying local forces, displacements and/or stresses will make the system evolve. At iteration i, and according to the prescribed boundary conditions, the nodes subjected to forces are displaced, causing deformation of the connected elements. Next, the homogeneous displacement field associated with the deformation of the elements is calculated. Then, the strain is derived from the linear displacement field using the kinematic equations for finite or infinitesimal strain. Using Hooke's law (Jaeger and Cook, 1979), the stress tensor is calculated for each triangular element. Nodal forces are then derived as a function of the element stress tensor. For infinitesimal deformation, tensors and forces are computed in the global coordinate system. For finite deformation, the displacement field, strain, and stress tensors are computed in the local coordinate system of each element to consider rigid-body rotation. Finally, the forces are rotated back to the global coordinate system, and contact forces are added for each node.

Contacts at Interfaces

Contacts are modeled using the concept of slave nodes and master segments (or master surfaces in 3-D), which is used in almost all FEM contact algorithms (Wriggers, 2002). Consider two fault blocks in contact. If a node of the interface mesh of one block penetrates a segment from the interface mesh of the second block, the node is considered a slave node, whereas the segment is considered a master segment. A contact force is then applied to push the node back toward the outside of the element containing the master segment. Thus, the contact force is directed toward the master segment along the normal to that segment. The master-slave concept implemented here allows nodes to be both slave nodes for an iteration and part of a master segment for other iterations. Therefore, to solve fault-block contact problems, it is not necessary to assign the master and slave roles to boundary surfaces.

Solving the System

The explicit solver is based on the Gauss-Seidel method, which allows nodal forces to be transmitted from node to node, until equilibrium is reached. Each node is treated independently from the others, and the order in which they are checked is irrelevant. Gauss-Seidel is an iterative method for solving partial differential equations on a triangulated surface (2-D) or tetrahedrized volume (3-D). When a node is checked, its new position depends on the current positions of the connected neighboring nodes (Figure 1). The key feature of this algorithm is that it uses new information, for instance, updated mesh node positions, as soon as they become available, as opposed to the Jacobi's method (Golub and Van Loan, 1996), in which the update of each node depends only on the values at neighboring nodes from the previous iteration.

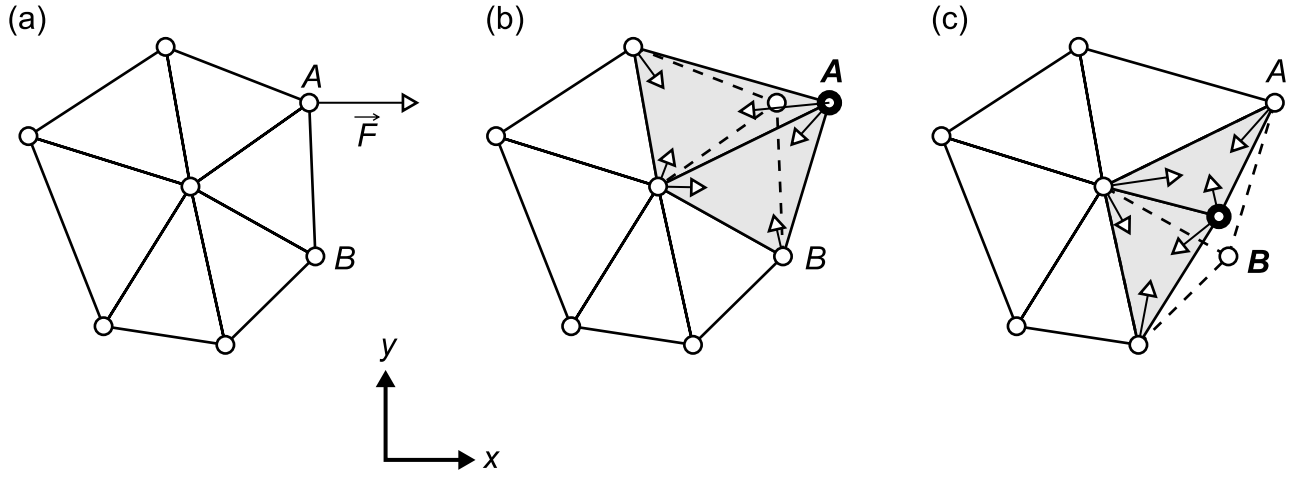

Figure 1. Iterative solver principle. (a) Initial mesh configuration with applied force $\vec{F}$ at node A. (b) At first iteration, node A is displaced according to force $\vec{F}$, and the two connected triangular elements are deformed accordingly. (c) At second iteration, node B is displaced according to the sum of forces, and the two connected triangular elements are deformed accordingly.

For a given node, we calculate the force resulting from the deformation of each connected element. The contact forces are then added. This force is then transformed back to a displacement vector using the nodal stiffness matrix. This matrix is defined as the sum of the stiffness matrices of the connected elements, for which the other nodes are considered fixed. Then, the displacement constraints or displacement boundary conditions, such as fixity, unfolding, and unfaulting, are applied to the computed displacement vector. Finally, the node is moved according to the new displacement vector, and the iteration jumps to the next node. The algorithm stops when the sum of the squared norm of the nodal displacement vector is below a given threshold value.

Advantages and Pitfalls

Linear elasticity is used as a tool for restoration because its fundamental properties are well suited for such modeling. It is the most intuitive mechanical behavior that provides a unique solution. Therefore, model results can easily be comprehended. Linear elasticity honors the full complement of physical laws that govern geological deformation, including conservation of momentum, mass, and energy. As a result, physical laws replace kinematic or geometric assumptions commonly used for restoring geological structures, such as preservation of segment length, surface area, or volume. Linear elasticity is reversible, which allows one to go back and forth from the restored to the initial state. Furthermore, because one commonly does not know the path of deformation that should be used for restoration, linear elasticity provides the simplest guess. Heterogeneous elastic properties are considered to honor vertical and lateral variations in rock rheology, which could have a significant effect on the restoration results (see below). In addition, mechanical boundary conditions can be prescribed using linear elasticity. For instance, there is no need to prescribe ad-hoc conditions such as a pin plane, a fixed transport direction, discontinuous rigid blocks, or fixed faults. Moreover, stress boundary conditions can be added to the model to consider the far-field tectonic stresses necessary for modeling structural heterogeneities (Maerten et al., 2002).

The main limitation of using linear elasticity is that we know from laboratory experiments (Jaeger and Cook, 1979) that rock does not behave as a perfectly elastic solid for all loading conditions. Indeed, nonlinear and nonrecoverable stress-strain relations are observed beyond the elastic limit. To some extent, these inelastic behaviors can be approximated by suitable reductions of the elastic stiffness and by introducing explicit displacement discontinuities into models that account, for example, for slip on faults.

Application to Restoration and Example Tests

We applied the FEM to restore a simple 2-D geological structure. The following examples illustrate the effectiveness of the method to treat contact interfaces and to model heterogeneous material properties. They highlight that different solutions are obtained even if the model's initial geometry is otherwise identical.

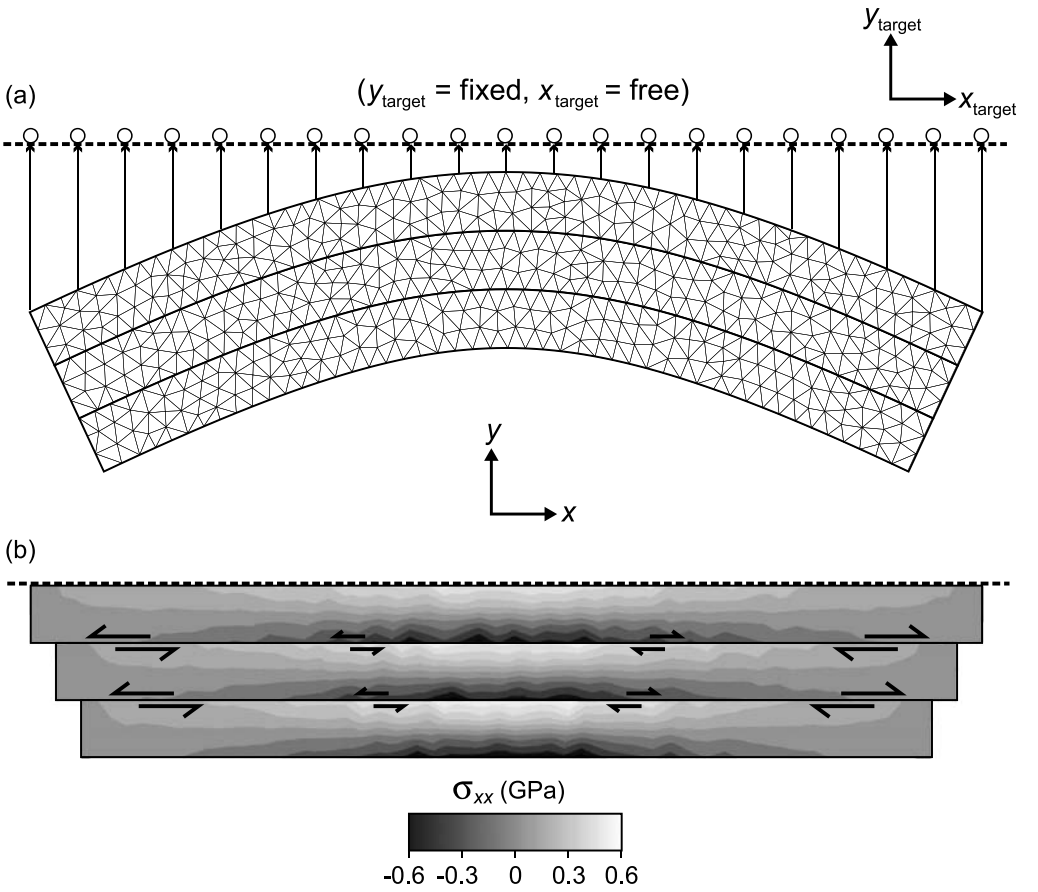

Figure 2. Restoration of a three-layer folded beam with bedding slip interfaces. (a) Mesh of the folded layers with homogeneous properties (E = 10 GPa, ν = 0.25). Slip is allowed between layer interfaces. (b) Isocontours of the computed σ_{xx}. Black is tension, and white is compression.

Model Configurations

Three model configurations, which consist of symmetric folds with constant thickness, have been investigated. The first is a three-layer model with bedding slip (Figure 2a). The modeled bedding interfaces can slip with no friction but are constrained to stay in mechanical contact to prevent any opening (i.e., gaps) and interpenetration (i.e., overlaps). In this configuration, the layers can mechanically interact, translate, rotate, and deform during the restoration. The mechanical properties of the model are homogeneous, with a Poisson's ratio of 0.25 and a Young's modulus of 10 GPa. The second configuration (Figure 3a) is a one-layer model with homogeneous material properties identical to the first configuration. The third configuration (Figure 3a) is a one-layer model in which a stiffer inclusion has been added. The mechanical properties of the inclusion are defined by a Poisson's ratio of 0.35 and a Young's modulus of 100 GPa, whereas the rest of the model is identical to the previous configurations. The base and the sides of the three models are free surfaces, and we use a finite plane-strain deformation.

The basic 2-D cross section restoration procedure consists of constraining each node of a stratigraphic horizon bounding a sedimentary layer (here the top one) to displace to a target curve (here horizontal) representing the depositional topography. Each of the displaced nodes is constrained to stay on the target curve but is free to move parallel to that curve. All the other nodes of the model, unless otherwise constrained, are free to move until the system converges and equilibrium is reached.

Results

The result of the first model (see Figure 2b) shows flat, restored layers with bedding slip that increases to the right and to the left side of the model and in opposite sense. The deformation is distributed among the three layers and produces bed-parallel compression and tension at the layer top and bottom, respectively. The unfolded lower layer is shorter than the unfolded upper layer, giving an overall inverted pyramid shape.

The single-layer model, however, gives notably different results (see Figure 3b). One still observes bed-parallel

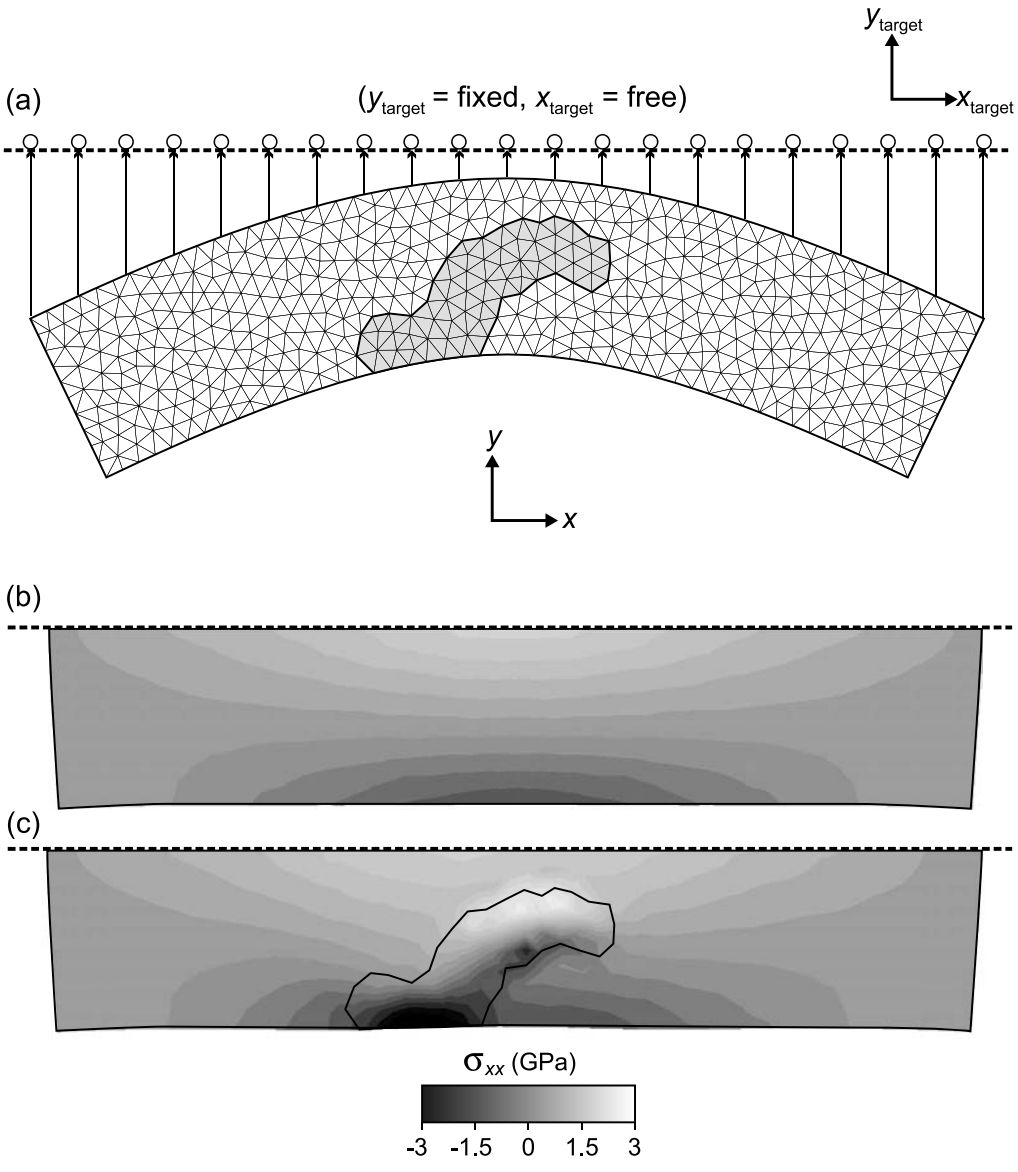

Figure 3. Restoration of a one-layer folded beam. (a) Mesh of the folded beam with location of an inclusion. (b) Isocontours of the computed σ_{xx} for a model with homogeneous properties (E = 10 GPa, ν = 0.25). (c) Isocontours of the computed σ_{xx} for a model with heterogeneous properties (E = 100 GPa, ν = 0.35 for the inclusion). Black is tension, and white is compression.

compression and tension at the layer top and bottom, respectively. However, the magnitude of the stress is about five times greater than that for the slipping layers because those layers are thinner: layer-parallel strain is proportional to the distance from the middle (neutral) surface of a bending layer, and the stress is proportional to the strain. Furthermore, the top boundary length is 2.3% shorter than that of the previous model, whereas the bottom boundary is 7.2% longer. Therefore, although the initial geometry is the same, the two first models give different restored geometries and different perturbed stress field distributions.

The purpose of the third model was to test the effect of heterogeneous material properties. The result (Figure 3c) shows that a stiffer inclusion perturbs the stress when the layer is unfolded. Near the top boundary of the inclusion, there is a large compression, whereas near the lower boundary, there is a large tension. The geometry of the restored fold is similar to the previous model. However, the bottom boundary of the fold is undulating instead of being straight as in the first and second models. For the following set of experiments, we use homogeneous material properties. Changing the homogeneous mechanical properties of a model will not significantly change the results, except for the computed stress magnitude, because stress is linearly dependent of the Young's modulus. As seen in Figure 3, only contrasts in mechanical properties would affect the results.

EXPERIMENT 1

We have evaluated the potential industry applications of this new technique by restoring a section across a laboratory experiment. This has many advantages over a natural example because (1) the initial and final configurations are known; (2) the complete kinematic and sediment deposition path is recorded; (3) the boundary conditions are well controlled; and (4) the mechanical properties are known. The analog modeling experiment analyzed in this section consists of a synsedimentary listric normal fault with a rigid footwall. Because of its quality and applicability, this model has already been used as a restoration case study (Bulnes and McClay, 1999; Erickson et al., 2000; Yamada and McClay, 2003). The laboratory experiment is described in McClay (1990); nonetheless, we summarize it in the following section for the sake of clarity.

Simple listric fault detachment surfaces were simulated using a molded footwall block above which a plastic sheet, attached to the moving wall, translates the hanging wall at a constant rate of 4.16×10^{-3} cm s^{-1} (1.63×10^{-3} in. s^{-1}) (see Figure 4a). The plastic sheet models a constant-displacement condition on the base of the model that implies a zero elongation parallel to the fault surface and a strong decollement surface (see Medwedeff and Krantz, 2002). The rigid nature of the footwall block means that the detachment surface has a constant geometry throughout the experiment, thus limiting the deformation to the hanging-wall block. Homogeneous dry quartz sand has been used to simulate the brittle behavior of the upper crust. Dry quartz sand (300 μm) has essentially linear Coulomb rheology with a friction angle of 31° (Ellis and McClay, 1988). During the 50% extension of the model, 28 sand layers with alternating colors were added incrementally to maintain a constant, horizontal upper free surface and to simulate synrift sedimentation that would infill an extensional basin. The serial section of the completed and impregnated model (Figure 4b) shows the well-established geometry of a rollover anticline. In this experiment, where the displacement is uniform over the entire fault surface, a crestal graben system is developed. The fault sequence diagram of Figure 4c shows the nucleation of new faults into this crestal graben.

Numerical Model Configuration

The geometry of the completed analog model was carefully interpreted, and a finite-element mesh model was built (Figure 5a), honoring the geometry of both the faults and the boundaries of the sediment layers. The synrift sequence has been divided into six packages, each with five increments of sedimentation, except for the youngest, which comprises three increments. These packages are used for the six-stage restoration models described below.

The mechanical properties throughout the model are homogeneous and are those of dry quartz sand, with a Poisson's ratio of 0.3, a Young's modulus of 2 MPa (Clark, 1966), and a friction angle of 31°. The base of the model is constrained to follow the shape of the fixed listric basal fault (see Figure 5b) with no constant slip imposed. Nodes of the base of the model can slide with no friction along the curved basal boundary to accommodate the displacement during the restoration and to mimic the sand-box model configuration. The modeled faults of the hanging-wall block can slip with no friction but are constrained to stay in mechanical contact, thus preventing any opening (i.e., gaps) and interpenetration (i.e., overlap) of the fault walls. This configuration allows a degree of freedom, where the faults can mechanically interact, translate, rotate, and deform during the restoration. The right side of the model is a free surface.

The restoration consists of sequentially removing the upper synrift sedimentary layer packages one by one and constraining the top of the next package to flatten along a horizontal target line. This target line (see Figure 5b) corresponds to the constant horizontal upper free surface of the analog model. The nodes can slide with no friction along the target line to accommodate the displacement during the restoration. For each stage of the restoration, all the nodes of the model are free to displace with respect to the constraints stated above, and the faults are free to accommodate any slip until the model equilibrates ($\Sigma F = 0$) and the energy is globally minimized. We assume a plane-strain model with no material motion in and out of the cross section. To simulate the flow behavior of the dry quartz sand approximately during the deformation, we set the accumulated stress to zero with no associated strain after each restoration stage, and the deformed geometry is used as input for the next restoration increment.

Restoration Results

We mapped the picture of the completed sand-box experiment onto the finite-element mesh using a texture mapping tool. This allows one to follow the deformation of the layers at each stage of the restoration. The results of the restoration are shown in Figure 6. The

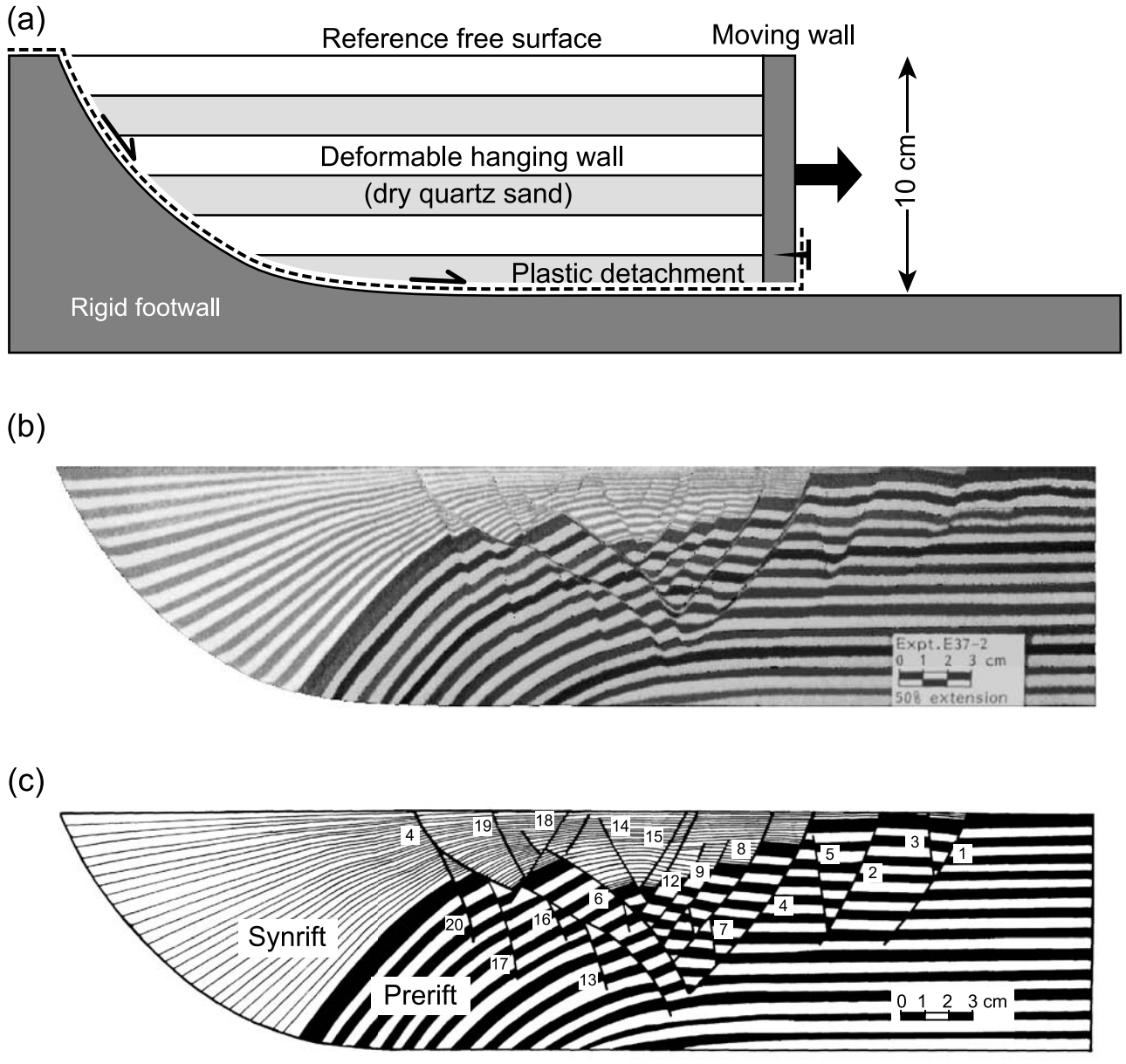

Figure 4. Physical experiment after McClay (1990). (a) Details of the model apparatus with a simple listric detachment formed by pulling the plastic sheet (attached to the moving wall) down and along the detachment surface. (b) Serial section of the impregnated sand model after 50% of extension. (c) Line drawing showing the deformed hanging wall and fault sequence inferred from sediment thickness variation.

faults located in the rollover anticline translate, rotate, and deform as the restoration sequence progresses, whereas faults located to the right in the model only exhibit a translation. The changes in fault crosscutting relationships through time, as observed in Figure 6 at intersections a and b, demonstrate how geomechanically based restoration can deal with complex fault geometry and interaction. For instance, the right-dipping fault of intersection b in Figure 6 crosscuts a left-dipping fault at stage 1, whereas it is the left-dipping fault that crosscuts the right-dipping fault at stage 2. These crosscutting relationships between faults help one understand the chronological development of faults that is described below.

When analyzing the evolution of the sand layers, one observes that they roll back along the basal listric fault to their original horizontal position, whereas the free right border of the model translates without any rotation. In the final restored state (stage 6 of Figure 6), the prerift beds are subhorizontal, which is consistent

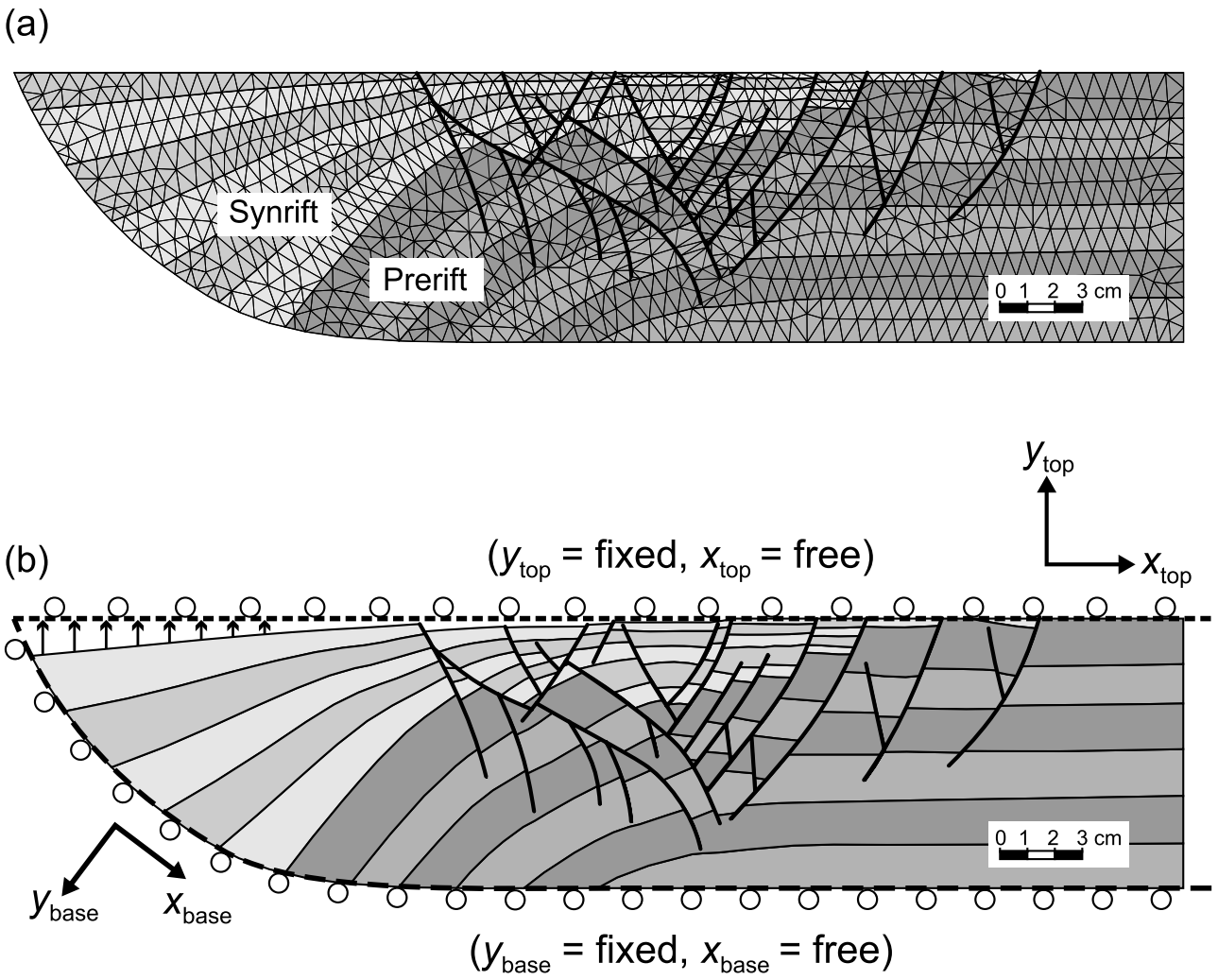

Figure 5. Configuration of the geomechanically based restoration. (a) Finite-element mesh (triangular elements) of the physical experiment with homogeneous properties (E = 2 MPa, ν = 0.3). (b) Boundary conditions constraining the base of the model to follow the shape of the fixed listric basal fault, the faults of the hanging-wall block to slip with no friction but to stay in mechanical contact, and the top of the model to flatten along a horizontal target line.

with the initial configuration of the physical sand-box experiment. However, close to the main bounding listric normal fault, some beds dip slightly to the left (~1.5°). Some mismatches also are seen in the continuity of the bedding interfaces across some of the faults. The origin of these discrepancies can cautiously be attributed to different sources. First, the mechanical behavior of the dry quartz sand might not be effectively modeled using elastic behavior. Second, remobilized sand close to the faults may be involved in normal or reverse drag attributed to inelastic deformation, which is not modeled. Third, we have not imposed a constant slip on the decollement as in the physical model. Finally, the plane-strain constraint used in the numerical model may not necessarily be appropriate. Indeed, some motion of the dry quartz sand parallel to the strike of the basal listric fault probably occurred during the physical experiment.

Each of the 28 synrift sand-layer increments of the physical experiment corresponds to 0.5 cm (0.2 in.) of displacement at a constant rate of 4.16×10^{-3} cm s^{-1} (1.63×10^{-3} in. s^{-1}). Therefore, one time increment is about 120 s. This time increment has been combined with the measure of shortening after each restoration stage to produce Figure 7. This graph compares the displacement rate imposed in the sand-box experiment with the displacement rate inferred from the restoration, and it provides a quantitative means for

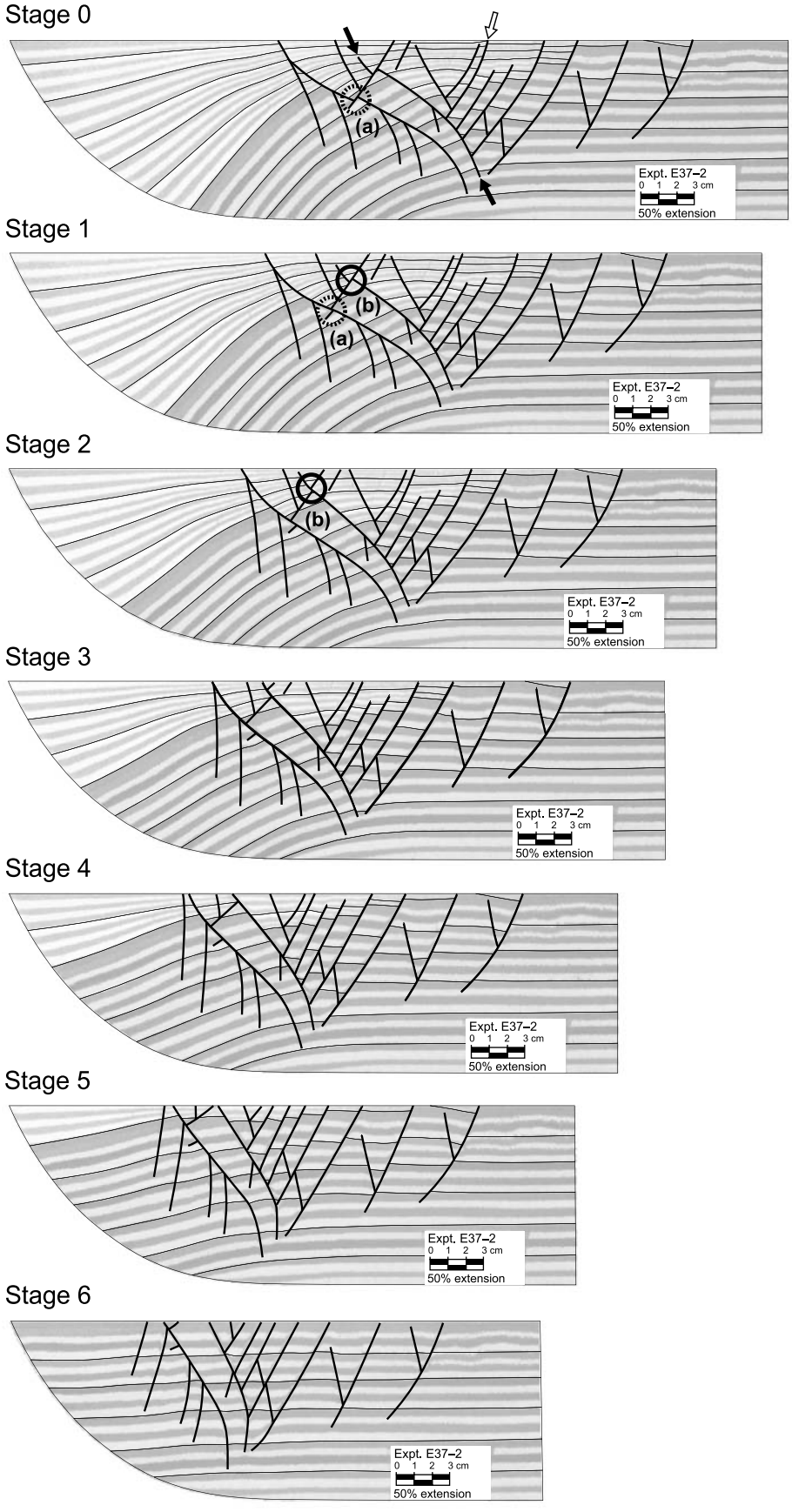

Figure 6. Results of the geomechanically based restoration from stages 0 to 6. The picture of the physical experiment section has been mapped onto the finite-element mesh. White arrow indicates the antithetic normal fault interacting with the studied fault (see Figure 8) marked with a black arrow. (a) and (b) indicate the locations of studied crosscutting relationships between intersecting faults.

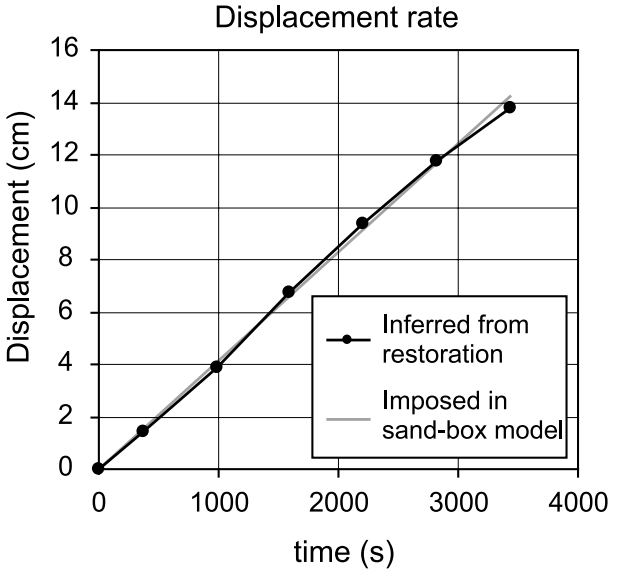

Figure 7. Graph comparing the displacement rate imposed in the sand-box experiment, with the displacement rate inferred from the restoration. The inferred displacement rate is constant and closely matches the one imposed in the sand-box experiment.

evaluating the restoration. The inferred displacement rate is constant and closely matches the one imposed in the sand-box experiment. The best linear fit is given by

$$y = 4.11 \times 10^{-3}x + 0.0248 \qquad (1)$$

with $R = 0.99915$ and where 4.11×10^{-3} is the computed displacement rate in centimeters per second.

Fault Development Analysis

For each restoration stage, we computed the slip distribution along the faults to estimate the amount of fault activity through time. Because there is no mesh regeneration between each restoration stage, we used the relative (x, y) coordinates of the nodes on both sides of the faults to compute the slip distribution along the faults. Cumulative slip distributions illustrate how the faults initiate, propagate, mechanically interact, and lock through time. As an example, Figure 8 shows, for each stage, the cumulative slip distribution along fault c, which is also marked by a black arrow in Figure 6 (stage 0). For the sake of simplicity, the modeled fault is analyzed in a forward sense.

Initially there is no slip along the fault c. Between stages 6 and 5, slip accumulates along the upper 6.5 cm (2.5 in.) of the fault. Little or no slip is computed along the lower 2 cm (0.8 in.) of the fault; therefore, the fault has not yet reached its final length. The fault propagates within the synrift sequence and offsets the top free surface as illustrated by the open slip distribution curve. Between stages 5 and 4, slip quickly accumulates along the fault, except in the lower centimeter. This highlights the highest intensity of fault activity, which clearly shows an asymmetric slip distribution with maximum slip near the top free surface as described in other studies (Childs et al., 1993; Maerten et al., 1999). Between stages 4 and 2, slip keeps accumulating, and the fault reaches its final length in both the postrift and the synrift sequence. At stage 2, the fault does not offset

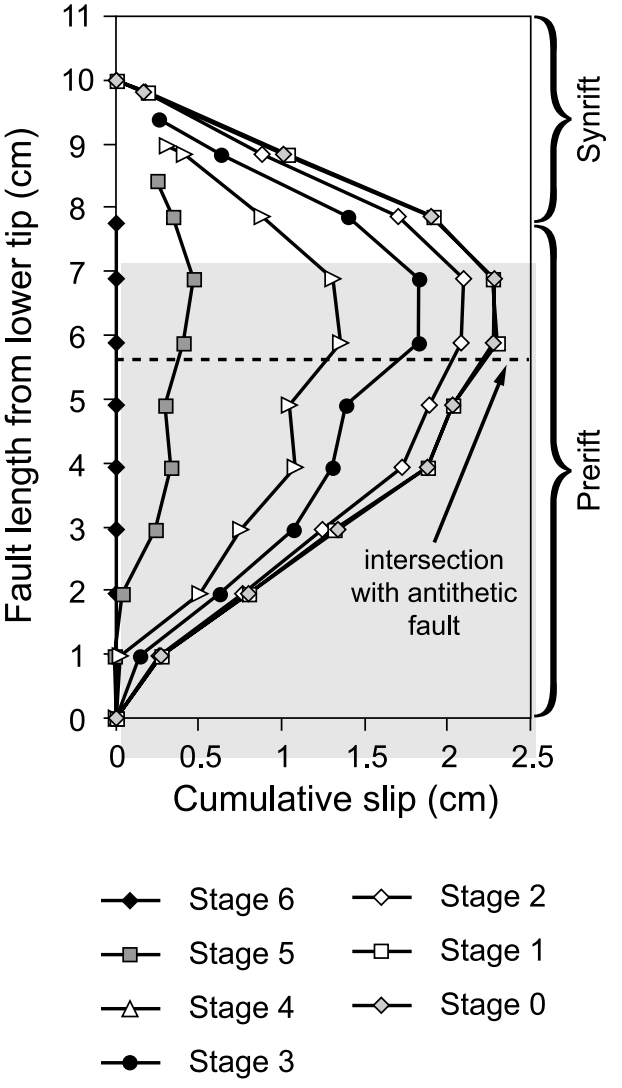

Figure 8. Cumulative slip distribution, for each stage of the restoration, computed along the fault marked as a black arrow in Figure 6. The dashed line locates the intersection with the mechanically interacting antithetic normal fault marked as a white arrow in Figure 6.

the top free surface as illustrated by the slip distribution that goes to zero in the synrift sequence. Between stages 2 and 1, slip accumulates everywhere except along the lower 2 cm (0.8 in.) of the fault, where the fault starts to lock. Between stages 1 and 0, the fault has entirely locked because no slip has accumulated. This corresponds to the change in fault crosscutting relationship observed in Figure 6b and described previously.

The dashed line of Figure 8 shows the location of the intersection, with a major antithetic fault marked by a white arrow in Figure 6 (stage 0). This fault mechanically interacts with the studied fault and perturbs its slip distribution as illustrated by a higher slip gradient. The fault interaction is the strongest between stages 5 and 3, where the slip gradient is the highest. This also corresponds to the highest activity of the antithetic intersecting fault. The perturbed slip distribution is consistent with previous independent observations (Nicol et al., 1995; Maerten, 2000) and mechanical analyses (Maerten et al., 1999). The mechanical interaction responsible for the perturbed slip distribution is attributed, at least in part, to elastic deformation that modifies the local shear stress acting on one fault as induced by slip on the other fault (Willemse, 1997; Maerten, 2000).

The entire model was analyzed in a forward sense to sequentially investigate the development of the faults in the hanging wall of the basal listric fault. Slip distribution along each fault was computed for each stage. It was then possible to infer the evolution of deformation, the propagation and locking history of the faults, and the fault chronology (see Figure 9).

Active Deformation Area

The analysis of fault development, which has been inferred from the computed fault-slip distributions, shows that through time, the deformation or fault activity is always localized close to the top free surface and just to the right of the base of the ramp (see Figure 9). This has been observed in many natural examples (Shelton, 1984; Williams and Vann, 1987) in sand-box experiments (Ellis and McClay, 1988; McClay, 1990; Withjack et al., 1995) and has been explained using elastic and elastoplastic geomechanical simulations (Erickson et al., 2001). The location and magnitude of the deformation is directly related to the shape of the basal listric normal fault that controls the rollover anticline geometry and, therefore, the distribution of the perturbed stress fields.

Fault Propagation

The analysis shows that faults initiate close to the top free surface and propagate downward in the prerift sequence and upward in the synrift sequence, as observed for faults a and c of Figure 9. The full length of the faults is attained at an early stage of the deformation. The analysis also shows that new active segments of the faults always form with a dip angle close to 60°. This is consistent with the Coulomb failure criterion (modified from Jaeger and Cook, 1979, p. 95), defined by

$$\tan(\pi - 2\delta) = \pm\frac{1}{\tan\varphi} \qquad (2)$$

where δ is the dip angle of the fault plane, φ is the friction angle, and with the maximum compressive stress (σ_{max}) vertical. This criterion predicts that for dry quartz sand ($\varphi = 31°$), $\delta = 60°$. The final observed S-shaped geometry of faults, a and c, can therefore be explained in part by the propagation of the faults upward and downward at 60° to the vertical as the model rotates over the listric normal fault (i.e., rollover anticline).

Locking Faults

Results from the fault-slip analysis illustrate how the faults start to lock. When a fault is fully developed, after initiating close to the top free surface and propagating downward in the prerift sequence, it starts to lock close to the base. Then, the locked segment of the fault spreads upward as seen for faults a and b (Figure 9). Another locking mechanism observed in the restoration occurs when a fault is crosscut by a propagating fault. This is clearly observed for faults a and c, locked by the propagating fault d (Figure 9).

Fault Chronology

The above observations based on the analysis of the computed fault-slip distributions permit one to infer the deformation and the fault development chronology of the entire model. This chronology is in good agreement with the chronology inferred from the sedimentation thickness variation analysis of the physical model (see Figure 4c). However, the geomechanical model adds more than a fault chronology based on sediment thickness analysis because it tells us when and where faults propagate and lock in space and through time.

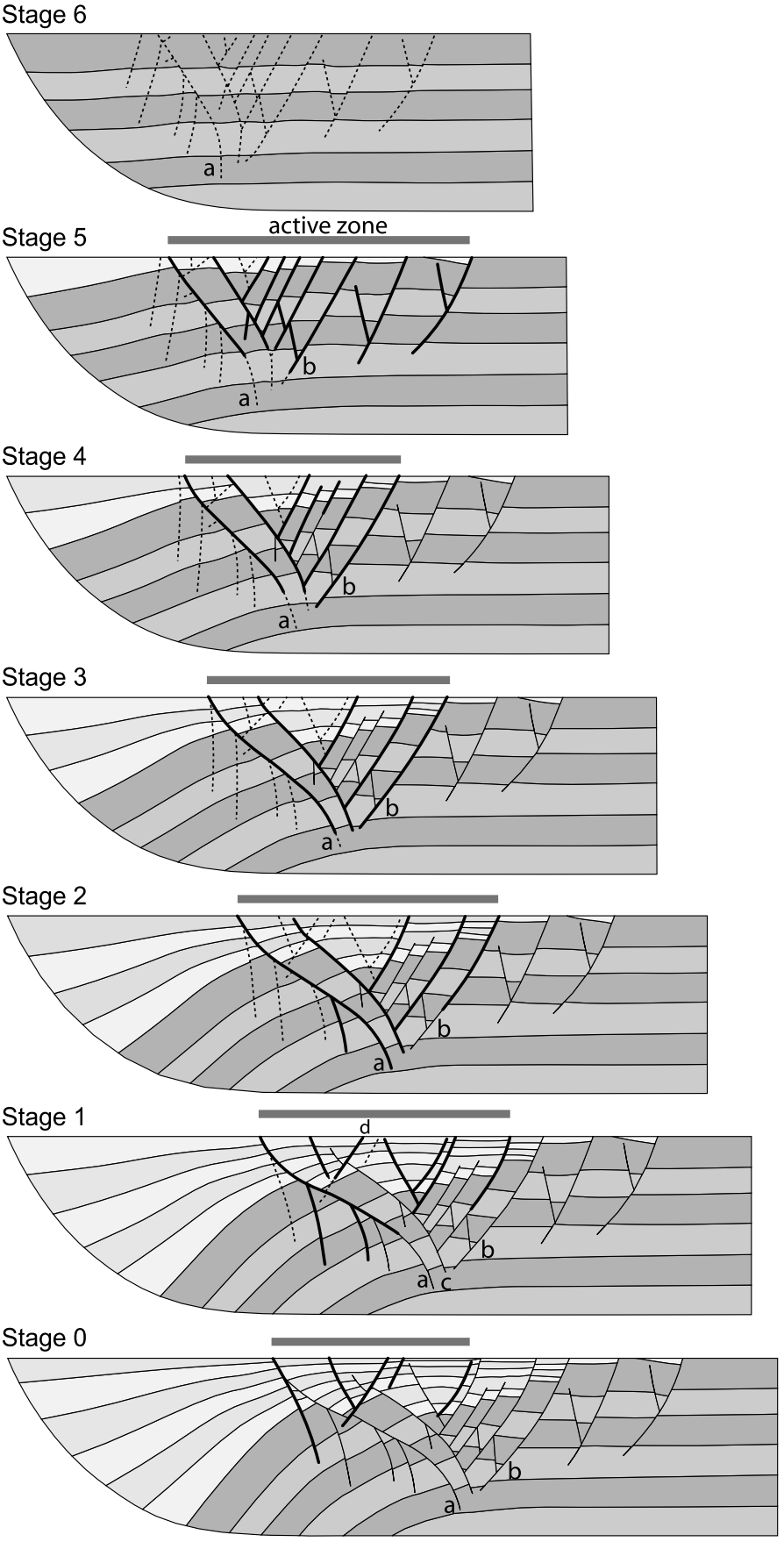

Figure 9. Sequential fault development analysis inferred from computed fault-slip distributions. Dashed faults are incipient faults, thick black faults are active faults, and thin black faults are locked. Faults marked as a, b, c, and d are referred in the text.

Conclusions and Applications to Reservoir Exploration and Production

The numerical model corresponds well to the physical model and provides additional insights about the physics of the process and quantitative values of physical parameters. The geomechanically based restoration provides a way to quickly and efficiently assess the development of the geological structures (i.e., faults) through time. This tool has significant potential for understanding complex geological structures and for evaluating hydrocarbon migration through time. Indeed, if one expects hydrocarbons to migrate along the active segments of faults, one could infer hydrocarbon-migration pathways directly and locate areas of potential structural traps that could be economically interesting.

EXPERIMENT 2

The objective of the following experiment is to predict fault location and geometry as observed in the physical model. Therefore, a model without the faults is restored, and attributes of the computed perturbed stress field are compared with the location and geometry of the faults, observable in the physical experiment.

Numerical Model Configuration

The geometry of the model corresponds to stage 0 of the previous experiment, where the first package of the synrift sequence has been removed (see Figure 10a, b). All the faults of the deformed hanging wall have been omitted, and the top boundary has been interpreted as a smooth surface without any offsets caused by the observed faults. This experiment could be viewed as a demonstration of how to interpret poor-quality seismic data, where faults cannot be detected from sedimentary interface offsets.

The mechanical properties throughout the model are homogeneous and similar to the previous experiment, with a Poisson's ratio of 0.3, a Young's modulus of 2 MPa, and a friction angle of 31°. The nodes at the base of the model are constrained to slide with no friction and to follow the shape of the fixed listric basal fault (see Figure 10b). The left side of the model is a free surface. The restoration consists of constraining the top of the model to flatten along the horizontal target line that corresponds to the constant horizontal upper free surface of the analog model. The nodes can slide with no friction along the target line to accommodate the displacement during the restoration. All the other nodes of the model are free to displace until the energy is globally minimized. We assume a plane-strain model with no material motion in and out of the cross section.

A second model (see Figure 11a), similar to the previous one, has been set up, in which the base has not been constrained to follow the listric fault. This experiment could be viewed as a demonstration of how to interpret poor-quality seismic data, where faults as well as the basal decollement cannot be detected.

Restoration Results

Based on the restoration boundary conditions and mechanical parameters, one computes the perturbed elastic stress field at the finite elements. Note that computed stresses are the stresses produced by restoring the model. The inverse of these stresses corresponds to the stresses that are computed if we deform the initial model geometry to the observed deformed geometry. Linear elasticity allows such back-and-forth analysis of the stresses from the deformed to the undeformed states. The principal stresses (i.e., inverse) are then combined with a failure criterion to create maps of both the predicted fault geometry and the predicted fault location.

The modeled fault geometry can be estimated using the Coulomb failure criterion defined in equation 2. Two conjugate failure planes intersect, and the fault dip angles are influenced only by the angle of friction φ and the orientation of the local maximum and minimum principal stresses, σ_{max} and σ_{min}, respectively. We chose the maximum Coulomb shear stress (MCSS) as an index for fault location because it has been effectively used by Maerten et al. (2002, in press) to model secondary normal faulting in a North Sea reservoir. The MCSS is the maximum shear stress that would occur on optimally oriented conjugate shear fractures as defined above. The value of the MCSS is determined by (Jaeger and Cook, 1979, p. 95):

$$\mathrm{MCSS} = \left(\frac{(\sigma_{max} - \sigma_{min})}{2}\sqrt{1 + \tan^2\varphi}\right) - \tan\varphi\left(\frac{(\sigma_{max} + \sigma_{min})}{2}\right) \quad (3)$$

where φ is the friction angle.

Figure 10c shows the contours of the MCSS over the entire model. The highest stress concentration is localized close to the top free surface and just to the

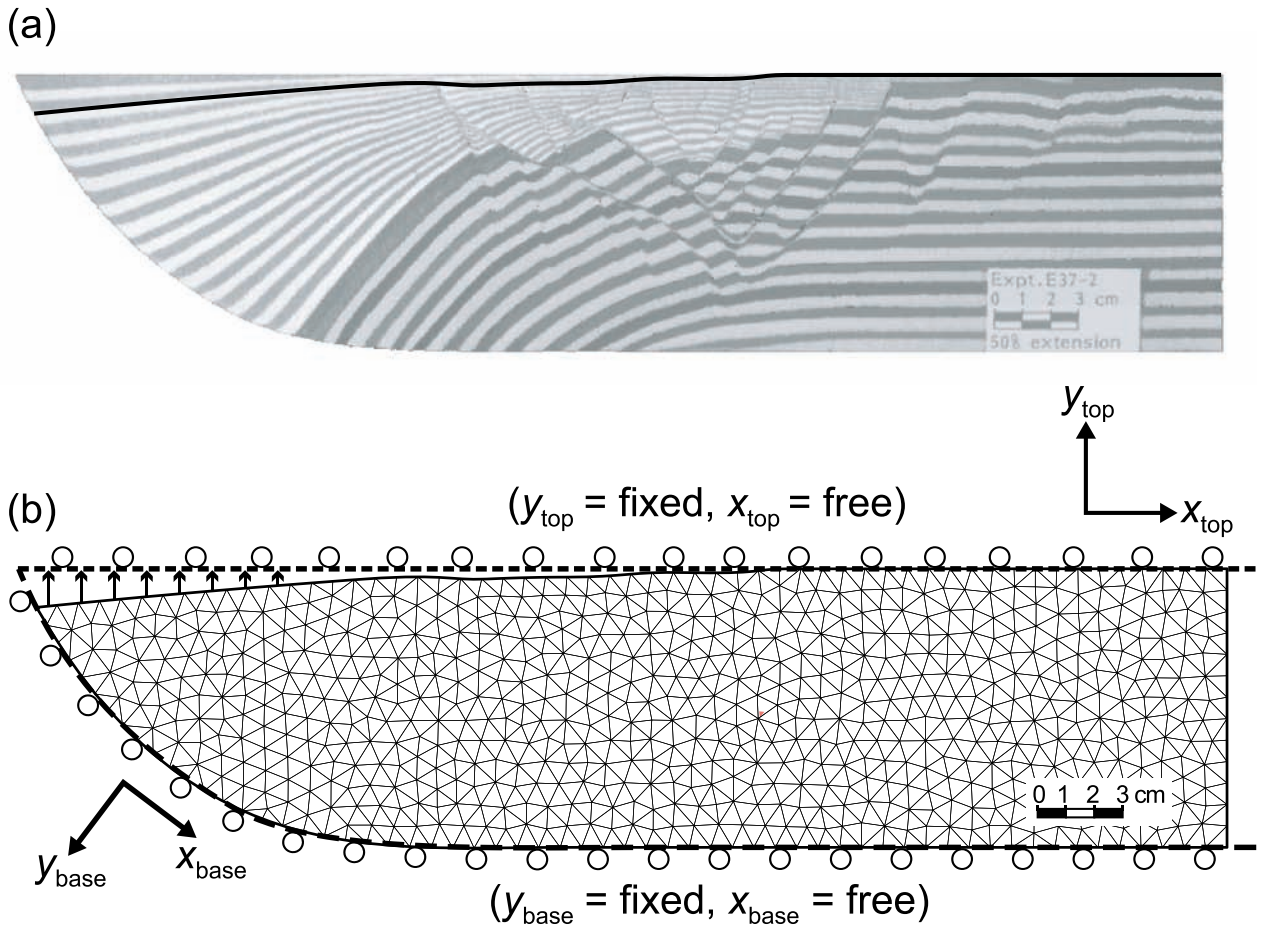
(a)
Expt.E37-2
0 1 2 3 cm
50% extension
(b)
y_{top}
x_{top}
(y_{top} = fixed, x_{top} = free)
0 1 2 3 cm
y_{base}
x_{base}
(y_{base} = fixed, x_{base} = free)
(c)
MCSS
high
low
(d)

right of the base of the ramp. This corresponds to the area of highest fault activity inferred from the previous restorations and is similar to the elastic and elastoplastic geomechanical simulations conducted by Erickson et al. (2001). The right side of the model displays the lowest MCSS stress values and corresponds to the region that has only been translated during the extension. When the active fault segments, predicted from stage 0 of the previous restoration experiment, are superimposed onto the map, they match with the highest computed MCSS values.

Figure 10d shows the orientation of the two shear failure planes derived from the computed stresses over the entire model. The sizes of the displayed shear planes are proportional to the computed MCSS. When the active faults, predicted from stage 0 of the previous restoration experiment, are superimposed onto the map, their geometry closely follows the curved path of the computed shear plane orientations.

Figure 11b also shows that without constraining the base of the model, the highest stress concentration still localizes close to the top free surface, which corresponds to the area of highest fault activity inferred from the previous restorations. Orientation of the two shear failure planes remains identical to the previous model close to the top free surface. However, the orientation of the conjugate shear planes tends to deviate from the previous model toward the traction-free base of the model.

Conclusions and Applications to Reservoir Exploration and Production

The geomechanically based restoration provides not only a complete and robust set of tools for inferring fault development chronology but also a tool to compute deformation between the restored and the deformed states. The analysis of deformation (i.e., perturbed stress field) can be used effectively in the oil industry to model undetected or subseismic faults (Maerten et al., 2002, in press). These predictions may serve to infer reservoir compartmentalization and to locate and exploit faulted regions of reservoirs.

EXPERIMENT 3

As an application of the geomechanically based restoration technique to model contractional structures, we restore a decameter-scale fold, which crops out in the Coulazou gully located near the Montpellier thrust fault, southern France (see Figure 12).

The Montpellier thrust fault is part of the thrusts and folds of the Pyrenean foreland (Arthaud and Séguret, 1981) formed during the Eocene. The thrusts were later truncated by north-south–striking extensional structures that developed throughout the late Oligocene–early Miocene rifting of the Gulf of Lion continental passive margin. The Mesozoic limestone cover, which was involved in thin-skinned compressional tectonics during the Pyrenean orogeny, outcrops in the Coulazou gully. The structural style of the area is characterized by a succession of approximately east-west–trending, decameter-scale folds affecting mechanical units of limestone layers that are several meters thick (Bazalgette, 2004). Figure 13 shows a fold cropping out along the cliff bounding the Coulazou gully and its interpretation in a vertical cross section. The fold has a gentle concave-downward shape affecting a 7–9-m (23–29-ft)-thick competent limestone unit vertically bounded by softer marly units. The lower marly calcareous unit, visible in the cross section, corresponds to a decollement level above which the fold has initiated. Layer-bounded mode I fractures cluster near the fold hinge. Field observations (Bazalgette, 2004) suggest that some of the fractures are reactivated pressure-solution surfaces, probably developed during the Pyrenean compression prior to folding.

Numerical Model Configuration

A finite-element mesh (Figure 14a) was developed from the interpretation of the fold that fits the geometry of the sedimentary layers. A finer mesh has been used near the hinge to honor the highest fold curvature geometry. The mechanical properties throughout the model are homogeneous and are those of limestone,

Figure 10. Model configuration and results of the second geomechanically based restoration. (a) Serial section of the impregnated physical experiment. The black line corresponds to the smoothed interpreted sedimentary layer without fault offsets. (b) Finite-element mesh with homogeneous properties (E = 2 GPa, ν = 0.3) and boundary conditions. The faults have been omitted in the model. (c) Isocontours of the computed maximum Coulomb shear stress (MCSS) resulting from the restoration and plotted over the initial unrestored geometry. (d) Orientation of the predicted shear plane scale to the MCSS. The size of the shear planes is proportional to the MCSS. Thick black lines are the superimposed active faults predicted from stage 0 of Figure 9. They closely matched the highest values of MCSS and the orientation of the computed shear planes.

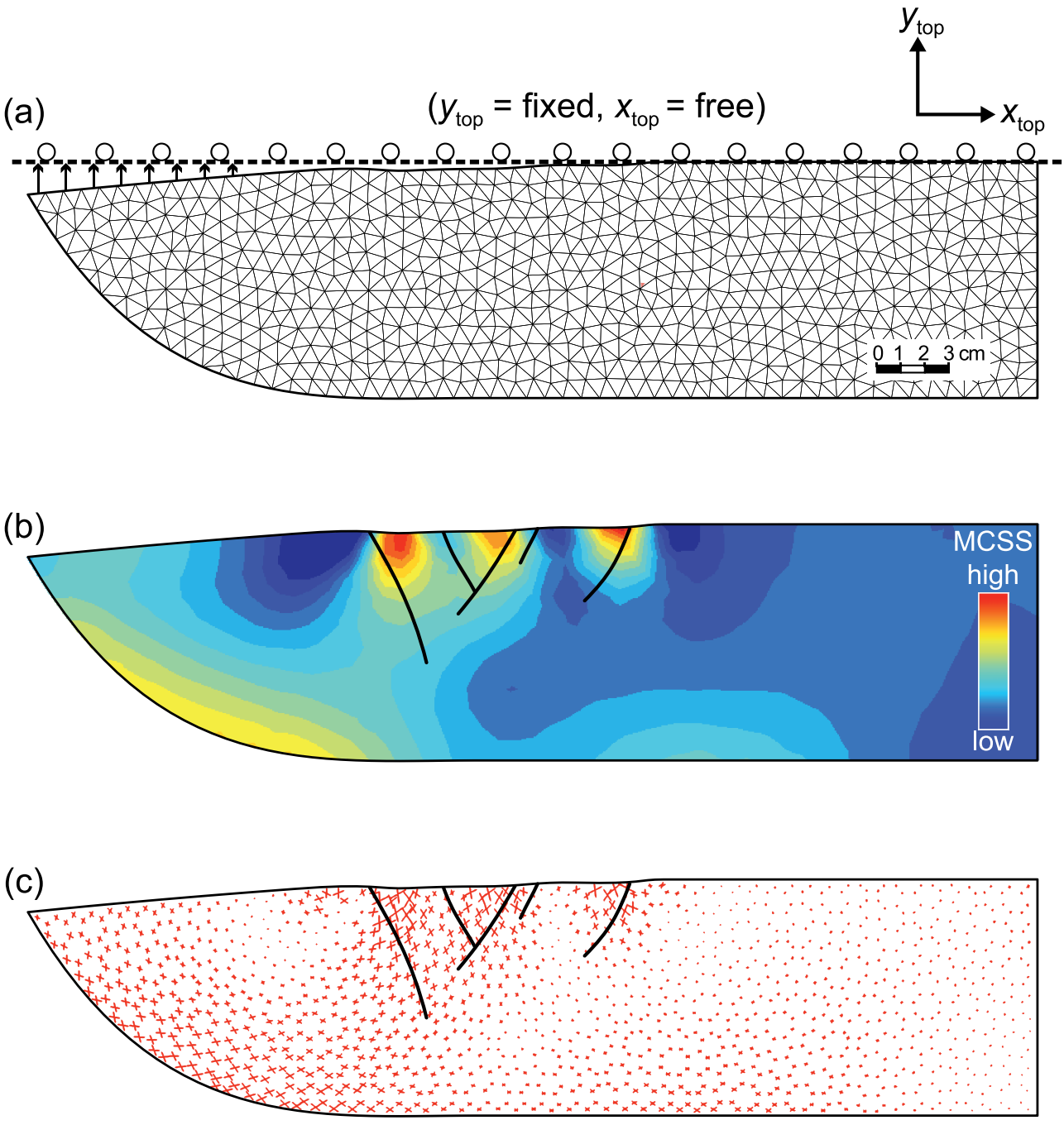

Figure 11. Model configuration and results of experiment 2 without constraining the base of the model. (a) Finite-element mesh with homogeneous properties (E = 2 GPa, ν = 0.3) and boundary conditions. The faults have been omitted in the model, and the base is free. (b) Isocontours of the computed maximum Coulomb shear stress (MCSS) resulting from the restoration and plotted over the initial unrestored geometry. (c) Orientation of the predicted shear planes scale to the MCSS. The size of the shear planes is proportional to the MCSS. Thick black lines are the superimposed active faults predicted from stage 0 of Figure 9.

with a Poisson's ratio of 0.25, a Young's modulus of 30 GPa (Clark, 1966).

The modeled bedding interfaces can slip with no friction but are constrained to stay in mechanical contact, thus preventing any opening and interpenetration of the layers. This configuration allows a degree of freedom where the layers can slip, translate, rotate, and deform during the restoration while they mechanically interact. The outside boundaries of the model are free surfaces. We justify the free lower and upper

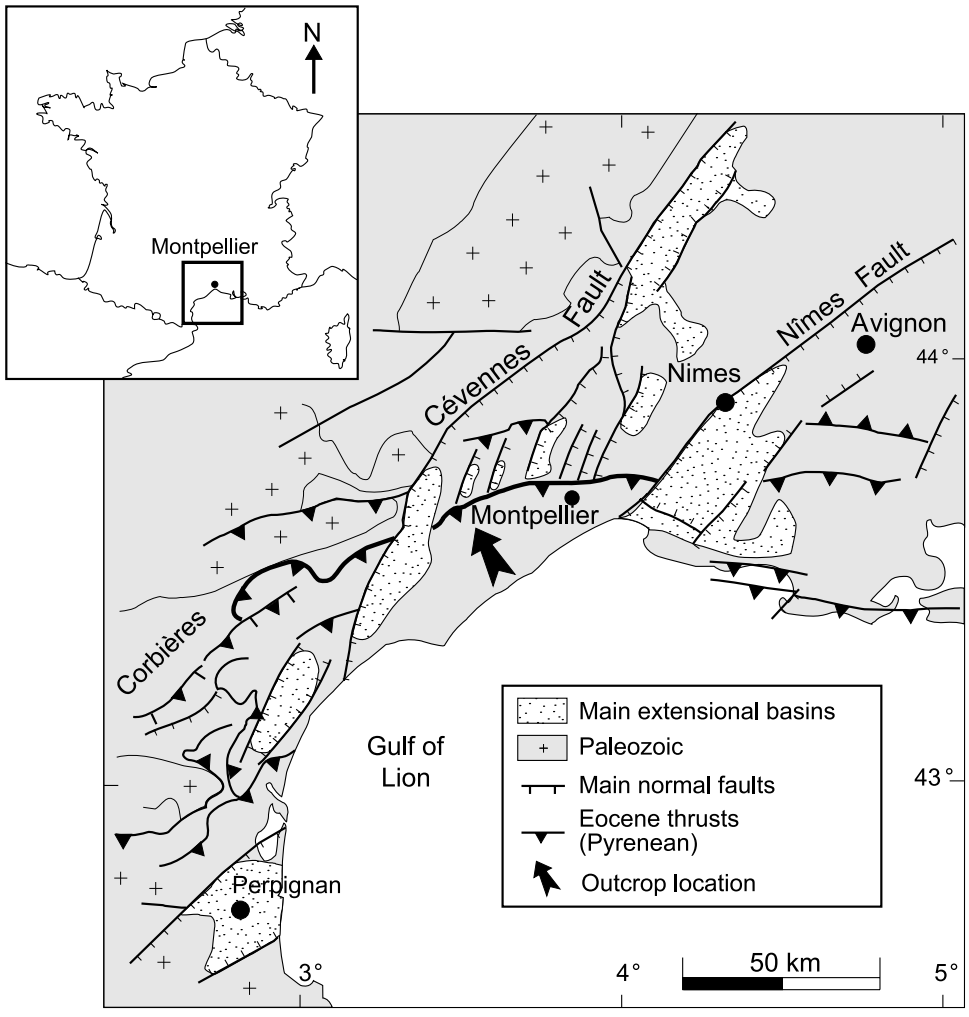

Figure 12. Simplified structural map of the central part of Gulf of Lion margin, showing the contractional and extensional structures, as well as the outcrop location. Paleozoic basement is marked with crosses.

boundaries by the fact that the mechanical competent limestone unit is bounded by softer marly layers, where decollement has probably occurred. In this example, the restoration consists of constraining all the nodes of the middle bedding interface to displace to a target horizontal line representing the hypothetical predeformed geometry (Figure 14b). Each of the displaced nodes can slide with no friction along the target line to accommodate the displacement during the restoration. All the other nodes of the model are free to move until equilibrium is reached. We assume a plane-strain model with no material motion in and out of the cross section.

Restoration Results

The result of the restoration (Figure 14c) shows subhorizontal layers with a constant thickness throughout the model. A small thickness variation with an increased thickness from north to south is present, which is also observed in the structural interpretation. This could be natural lateral thickness variation or artificial variation caused by the imperfect perpendicularity between the camera direction and the cliff face (i.e., perspective distortion). Slip occurred in all bedding interfaces, giving an overall inverted pyramid shape as observed in the synthetic example of Figure 2, where the unfolded lower layers are shorter than the unfolded upper layers.

We mapped both the outcrop image of the fold and the fracture interpretation (Figures 15, 16) onto the finite-element mesh to display the observed fractures and bedding interfaces of the structure in what could have been its predeformed geometry. They show rotated fractures that appear perpendicular to bedding.

For the sake of clarity, the stress displayed in Figure 16 (i.e., least principal stress σ_3) is the stress produced by folding the beds. The inverse of that stress corresponds to the maximum compressive stress (σ_1) that is computed by unfolding the beds to subhorizontal

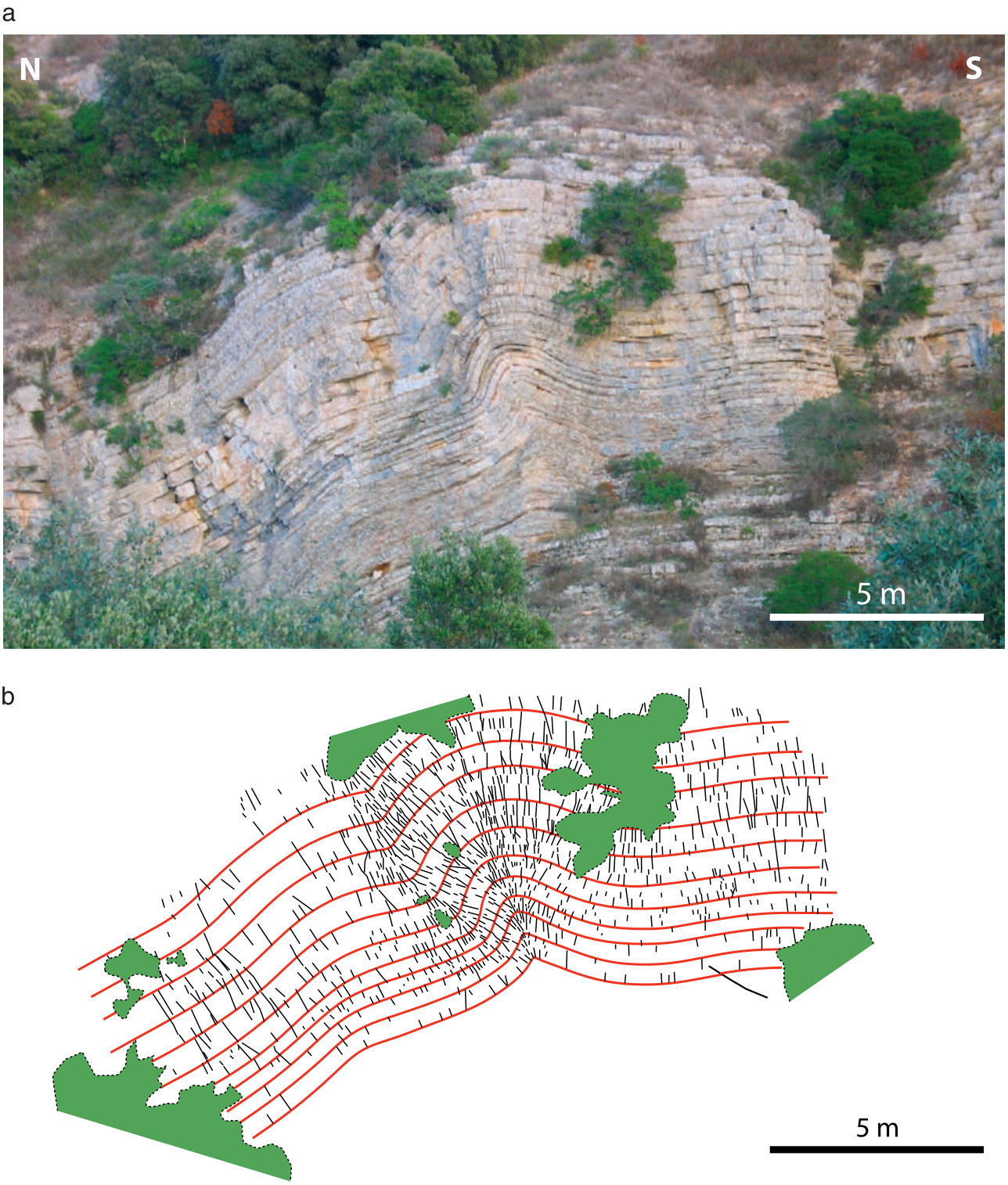

Figure 13. Contractional fold of the Coulazou gully, southern France. (a) Outcrop photograph. (b) Structure interpretation showing the main bedding interfaces and the observed fractures.

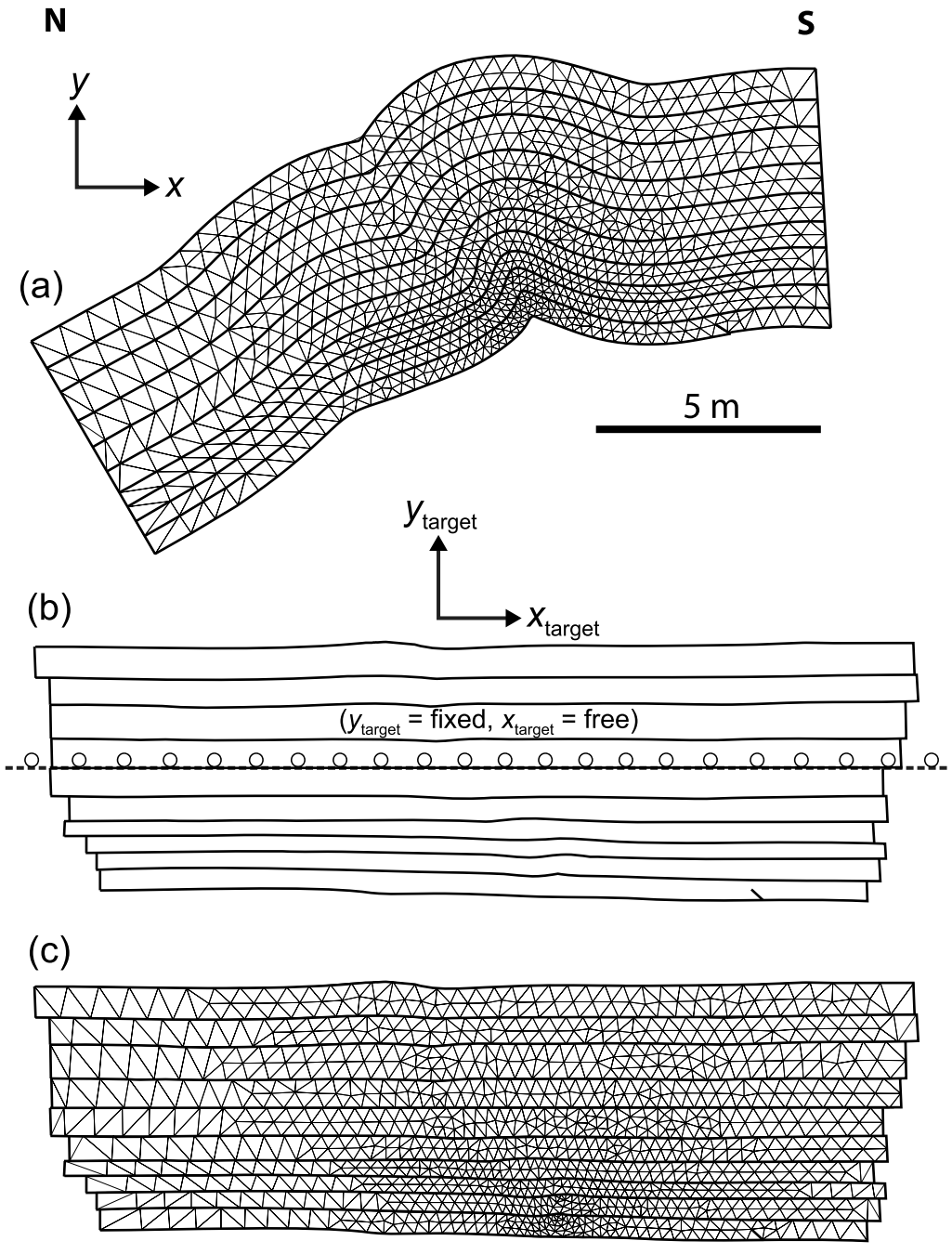

Figure 14. Model configuration of the contractional fold restoration. (a) Finite-element mesh (triangular elements) with homogeneous properties (E = 30 GPa, ν = 0.25). (b) Boundary conditions constraining the middle bedding interface of the model to flatten along a horizontal target line. The boundary conditions are sketched on the unfolded model for clarity. (c) Unfolded finite-element mesh.

beds. The deformation caused by the folding is distributed among the 10 layers and produces bed-parallel tension and compression at the layer top and bottom, respectively. Results show stress concentrations (tension) localized along the fold hinge and articulations and in the extrados of the folds, which reasonably correlate with the location of the observed fracture clusters. The restoration produces bed-parallel tension that could ultimately reactivate preexisting bed-perpendicular stylolites or develop joints (opening-mode fractures) normal to bedding, as observed in Figure 16a and b. The high stress concentration magnitude computed from the unfolding can be explained by the fact that stresses that exceed the elastic limit, and would be subject to nonlinear elastic deformation, are not considered. We would expect fractures developing in such areas in response to the stress concentration. Note that no far-field tectonic stresses have been added to the model; therefore, the computed stresses only reflect the deformation caused by unfolding.

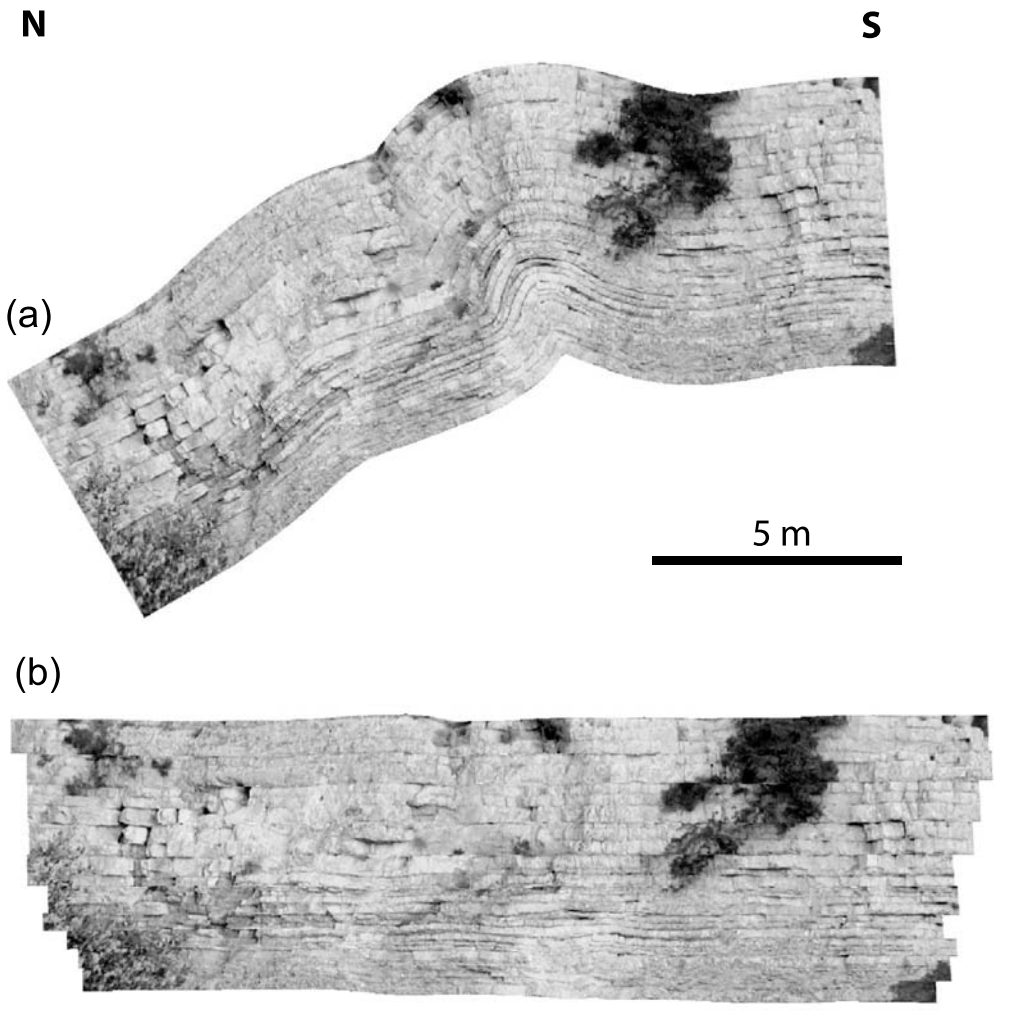

Figure 15. Results of the geomechanically based restoration. (a) The outcrop photograph has been mapped onto the finite-element mesh. (b) Unfolded photograph showing subhorizontal beds.

Figure 17 shows the quantitative comparison between fracture frequency (i.e., fractures per meter) measured along three beds and computed stress σ_3 along the same beds. The maximum fracture frequency matches the location of the highest value of σ_3 for the three layers. The asymmetric nature of fracture frequency with higher frequency to the left of the maximum is reproduced for layers A and B. Layer C displays a symmetric fracture frequency graph that is also reproduced by the restoration.

Conclusions and Applications to Reservoir Exploration and Production

We have shown that the geomechanically based restoration technique can be applied to restore both extensional and contractional structures. The technique provides a robust tool for efficiently modeling diffuse deformation (i.e., undetected joints) from the computed stress field. These modeling efforts may serve to locate and exploit fractured regions of reservoirs.

CONCLUSIONS

The restoration method presented here combines fundamental physical laws that govern rock deformation, including conservation of momentum and mass, with the kinematic constraints necessary for restoring geological structures. The physical laws and linear elastic theory replace ad-hoc kinematic and geometric assumptions commonly used by other methods, including preservation of segment length, area, or volume. The main benefits of such an approach follow: (1) rock mechanical properties and their variation throughout the geological model are considered; (2) the mechanical interaction

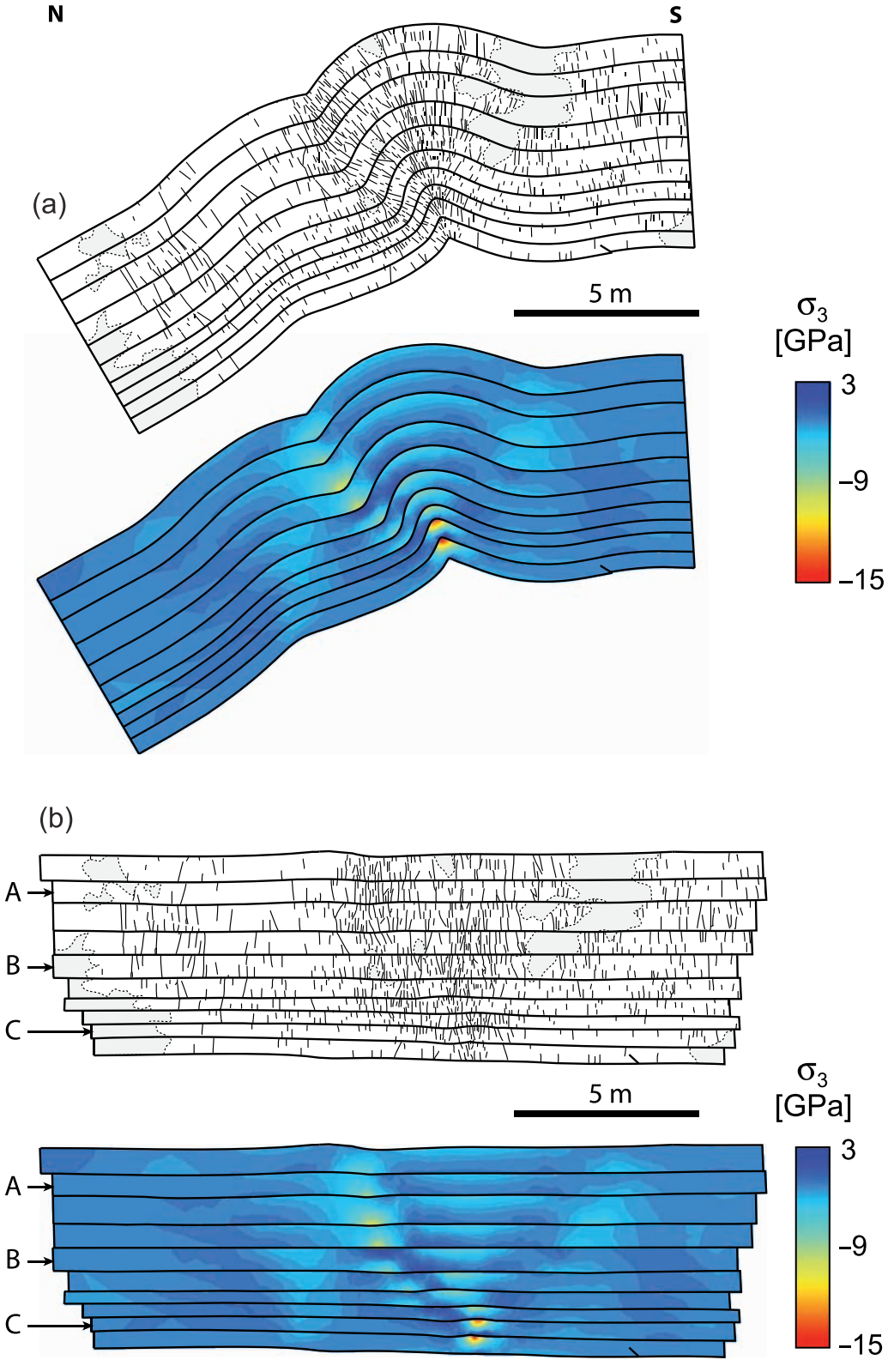

Figure 16. Comparison between observed fractures and computed stress. (a) Observed fractures and isocontours of the computed least principal stress (σ_3) resulting from the restoration and plotted over the initial unrestored geometry. (b) Observed fractures and isocontours of computed σ_3 on the actual fold geometry. Note that σ_3 is the stress produced by folding the beds. The inverse of that stress corresponds to the maximum principal stress (σ_1) that is computed when we restore the folded beds to the subhorizontal beds. Fracture closely matched the highest values of σ_3. A, B, and C represent the graphs of Figure 17.

of faults and slipping bedding surfaces is modeled; and (3) the method applies the same principles to restore geological structures from any tectonic setting. In contrast, kinematic and geometric models typically adopt different mechanisms and constraints to mimic the deformation in different tectonic settings. In addition, this

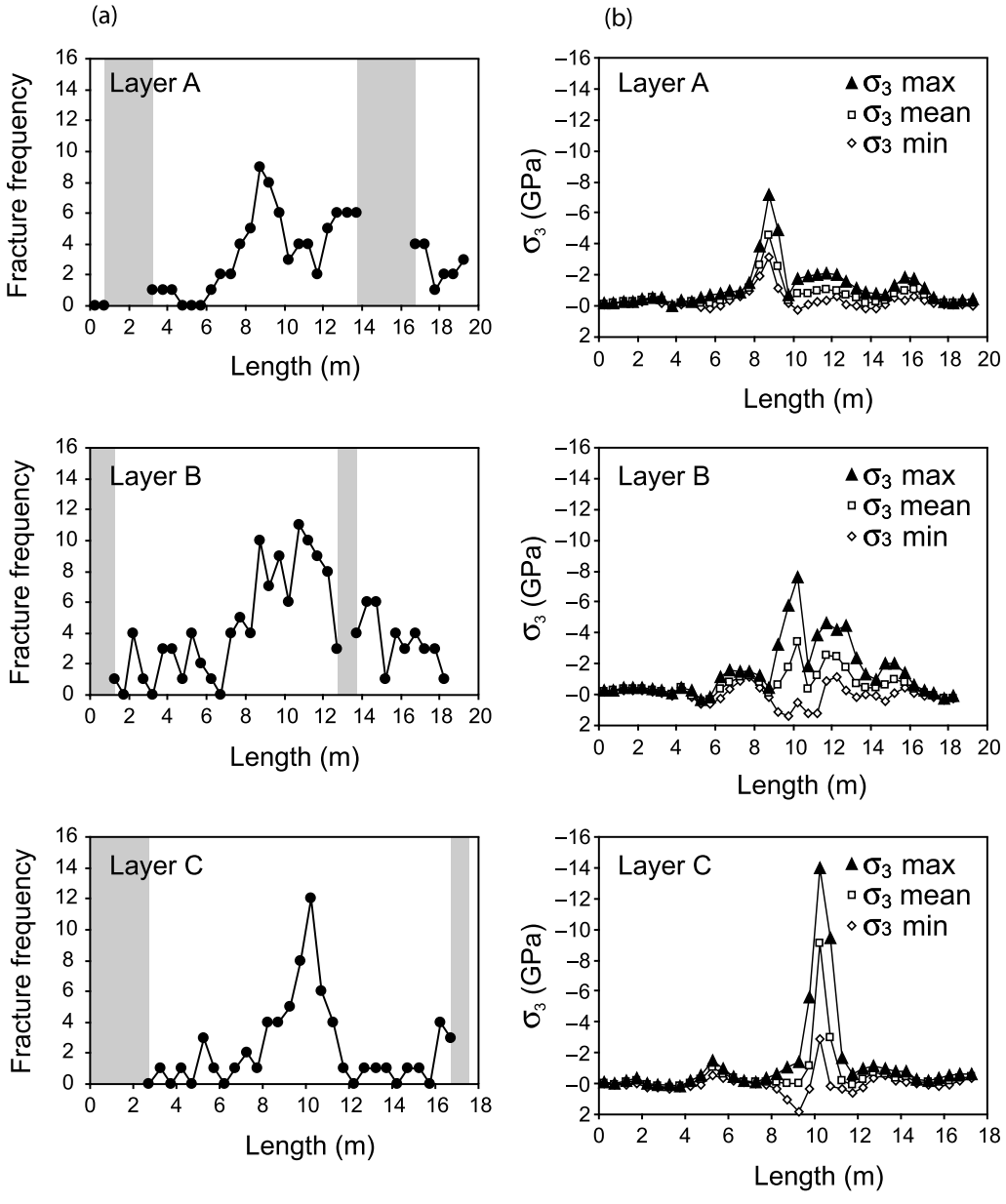

Figure 17. Comparison between observed fractures and computed stress. (a) Observed fracture frequency (i.e., fracture per meter) for three different layers, A, B, and C. Gray bands are areas of no data because of vegetation. (b) Computed σ_3 along the three layers A, B, and C. Fracture frequency closely matched the values of the least principal stress σ_3.

method computes stresses from the restoration, and these can be related to small-scale structural heterogeneities (i.e., subseismic faults and joints).

The results of this study have shown that the geomechanically based restoration approach, despite its limitations in terms of inelastic deformation, allows one to successfully model fault chronology as well as small-scale joints during restoration. We have demonstrated, through the restoration of sand layers in a laboratory experiment, that the approach provides an efficient way to assess fault development through time. We suggest that the approach could have significant potential for evaluating hydrocarbon-migration pathways through time and for locating structural traps. Using the same example, we have demonstrated that such an approach could be used in the oil industry to model subseismic faults. These predictions may serve to infer reservoir compartmentalization and to locate and exploit faulted regions of reservoirs.

Finally, we have shown that this restoration technique can be applied to restore contractional structures, and that it provides a robust tool for efficiently modeling diffuse deformation (i.e., jointing) necessary to exploit fractured reservoirs. Geological restoration based on geomechanics appears a promising route toward improved reservoir characterization.

REFERENCES CITED

Arthaud, F., and M. Séguret, 1981, Les structures pyrénéennes du Languedoc et du Golfe du Lion (Sud de la France): Bulletin de la Société Géologique de France, v. 23, p. 51–63.

Bai, T., L. Maerten, M. R. Gross, and A. Aydin, 2002, Orthogonal cross joints: Do they imply a regional stress rotation?: Journal of Structural Geology, v. 24, p. 77–88.

Bazalgette, L., 2004, Relations plissement/fracturation multi échelle dans les multicouches sédimentaires du domaine élastique/fragile: Accommodation discontinue de la courbure par la fracturation de petite échelle et par les articulations. Possibles implications dynamiques dans les écoulements des réservoirs: Thèse de Doctorat, Université de Montpellier, France, 252 p.

Bourne, S. J., and E. J. M. Willemse, 2001, Elastic stress control on the pattern of tensile fracturing around a small fault network at Nash Point, U.K.: Journal of Structural Geology, v. 23, p. 1753–1770.

Bourne, S. J., A. Rijkels, B. J. Stephenson, and E. J. M. Willemse, 2000, Predictive modeling of naturally fractured reservoirs using geomechanics and flow simulation: GeoArabia, v. 6, no. 1, p. 87–102.

Bulnes, M., and K. McClay, 1999, Benefits and limitations of different 2D algorithms used in cross-section restoration of inverted extensional faults: Application to physical experiments: Tectonophysics, v. 312, p. 175–189.

Childs, C., J. J. Walsh, and J. Watterson, 1990, A method for estimation of the density of fault displacements below the limits of seismic resolution in reservoir formations, *in* G. Trotman, ed., North Sea oil and gas reservoirs: Liverpool, The Norwegian Institute of Technology, v. 2, p. 193–203.

Childs, C., S. J. Easton, B. C. Vendeville, M. P. A. Jackson, S. T. Lin, J. J. Walsh, and J. Watterson, 1993, Kinematic analysis of faults in a physical model of growth faulting above a viscous salt analogue: Tectonophysics, v. 228, p. 313–329.

Clark, S. P., Jr., ed., 1966, Handbook of physical constants (revised edition): Geological Society of America Memoir 97, 587 p.

Dahlstrom, C. D. A., 1969, Balanced cross section: Canadian Journal of Earth Sciences, v. 6, p. 743–757.

Davatzes, N. C., P. Eichhubl, and A. Aydin, 2005, Structural evolution of fault zones in sandstone by multiple deformation mechanisms: Moab fault, southeast Utah: Geological Society of America Bulletin, v. 117, p. 135–148.

Davison, I., 1986, Listric normal fault profiles: Calculation using bed-length balance and fault displacement: Journal of Structural Geology, v. 8, p. 209–210.

Dokka, R. K., and C. J. Travis, 1990, Late Cenozoic strike-slip faulting in the Mojave Desert, California: Tectonics, v. 9, p. 311–340.

Dorn, G. A., 1998, Modern 3D seismic interpretation: The Leading Edge, v. 17, p. 1262–1272.

Dula, W. F., 1991, Geometric models of listric normal faults and rollover folds: AAPG Bulletin, v. 75, p. 1609–1625.

Dunbar, J. A., and R. W. Cook, 2003, Palinspastic reconstruction of structure maps: An automated finite element approach with heterogeneous strain: Journal of Structural Geology, v. 26, p. 1021–1036.

Ellis, P. G., and K. McClay, 1988, Listric extensional fault system—Results of analogue model experiments: Basin Research, v. 1, p. 55–70.

Erickson, G. S., L. M. Strayer, and J. Suppe, 2001, Mechanics of extension and inversion in the hanging walls of listric normal faults: Journal of Geophysical Research, v. 106, p. 26,655–26,670.

Erickson, S. G., S. Hardy, and J. Suppe, 2000, Sequential restoration and unstraining of structural cross sections: Application to extensional terranes: AAPG Bulletin, v. 84, p. 234–249.

Gauthier, B. D. M., and S. D. Lake, 1993, Probabilistic modeling of faults below the limit of seismic resolution in Pelican field, North Sea, offshore United Kingdom: AAPG Bulletin, v. 77, p. 761–776.

Gibbs, A. D., 1983, Balanced cross-section construction from seismic sections in areas of extensional tectonics: Journal of Structural Geology, v. 5, p. 153–160.

Gillespie, P. A., C. Howard, J. J. Walsh, and J. Watterson, 1993, Measurement and characterisation of spatial distributions of fractures: Tectonophysics, v. 226, p. 113–141.

Golub, G. H., and C. F. Van Loan, eds., 1996, Matrix computations: Johns Hopkins Series in the Mathematical Sciences, 3d ed.: Baltimore, Maryland, Johns Hopkins University Press, v. 3, 694 p.

Gratier, J.-P., B. Guillier, A. Delorme, and F. Odonne, 1991, Restoration and balance of a folded and faulted surface by best-fitting of finite elements: Principle and applications: Journal of Structural Geology, v. 13, p. 111–115.

Griffiths, P., J. Serena, N. Slater, F. Schaefer, R. Osfield, and H. Reiser, 2002, A new technique for 3-D flexural-slip restoration: Journal of Structural Geology, v. 24, p. 773–782.

Guiton, M. L. E., 2001, Contribution of pervasive fractures to the deformation during folding of sedimentary rocks: Thèse de Doctorat, École Polytechnique, Paris, France, 255 p.

Guiton, M. L. E., Y. M. Leroy, and W. Sassi, 2003a, Activation of diffuse discontinuities and folding of sedimentary layers: Journal of Geophysical Research, v. 108, p. 2183, doi:10.1029/2002JB001770.

Guiton, M. L. E., W. Sassi, Y. M. Leroy, and B. D. M. Gauthier, 2003b, Mechanical constraints on the chronology of fracture activation in folded Devonian sandstone of the western Moroccan Anti-Atlas: Journal of Structural Geology, v. 25, p. 1317–1330.

Hauge, T. A., and G. G. Gray, 1996, A critique of techniques for modelling normal-fault and rollover geometries, *in* P. G. Buchanan and D. A. Nieuwland, eds., Modern developments in structural interpretation, validation and modelling: Geological Society (London) Special Publication, v. 99, p. 89–97.

Healy, D., G. Yielding, and N. Kusznir, 2004, Fracture prediction for the 1980 El Asnam, Algeria earthquake via elastic dislocation modeling: Tectonics, v. 23, p. 1–21.

Hennings, P. H., J. E. Olson, and L. B. Thompson, 2000, Combining outcrop data and three-dimensional structural models to characterize fractured reservoirs: An example from Wyoming: AAPG Bulletin, v. 84, p. 830–849.

Hossack, J. R., 1979, The use of balanced cross section in the calculation of orogenic contraction: A review: Journal of the Geological Society (London), v. 136, p. 705–711.

Hughes, T. J. R., 1987, The finite element method: Linear static and dynamic finite element analysis: New Jersey, Prentice-Hall, 803 p.

Jaeger, J. C., and N. G. W. Cook, 1979, Fundamentals of rock mechanics: New York, Chapman and Hall, 249 p.

Kattenhorn, S. A., A. Aydin, and D. D. Pollard, 2000, Joints at high angles to normal fault strike: An explanation using 3-D numerical models of fault-perturbed stress fields: Journal of Structural Geology, v. 22, p. 1–23.

Kerr, H., N. White, and J.-P. Brun, 1993, An automatic method for determining 3-D normal fault geometry: Journal of geophysical Research, v. 98, p. 17,837–17,857.

Lévy, B., 2000, Topologie algorithmique combinatoire et plongement: Ph.D. thesis, University of Nancy, Nancy, France, 190 p.

Maerten, L., 1999, Mechanical interaction of intersecting normal

faults: Theory, field examples and applications: Ph.D. thesis, Stanford University, Stanford, California, 167 p.

Maerten, L., 2000, Variation in slip on intersecting normal faults: Implications for paleostress inversion: Journal of Geophysical Research, v. 105, p. 25,553–25,565.

Maerten, L., M. J. Willemse, D. D. Pollard, and K. Rawnsley, 1999, Slip distributions on intersecting normal faults: Journal of Structural Geology, v. 21, p. 259–271.

Maerten, L., P. Gillespie, and D. D. Pollard, 2002, Effect of local stress perturbation on secondary fault development: Journal of Structural Geology, v. 24, p. 145–153.

Maerten, L., P. Gillespie, and J.-M. Daniel, in press, 3-D geomechanical modeling for constraint of subseismic fault simulation: AAPG Bulletin, v. 90.

McClay, K. R., 1990, Extensional fault systems in sedimentary basins: A review of analogue model studies: Marine and Petroleum Geology, v. 7, p. 206–233.

Medwedeff, D. A., and R. W. Krantz, 2002, Kinematic and analog modeling of 3-D extensional ramps: Observations and a new 3-D deformation model: Journal of Structural Geology, v. 24, p. 763–772.

Nicol, A., J. J. Walsh, J. Watterson, and P. G. Bretan, 1995, Three-dimensional geometry and growth of conjugate normal faults: Journal of Structural Geology, v. 17, p. 847–862.

Novozhilov, V. V., 1953, Foundations of the nonlinear theory of elasticity: Rochester, New York, Graylock Press.

Rouby, D., P. R. Cobbold, P. Szatmari, S. Demerican, D. Coelho, and J. A. Rici, 1993, Least-squares palinspastic restoration of region of normal faulting— Application to the Campos Basin (Brasil): Tectonophysics, v. 221, p. 439–452.

Rouby, D., H. Xiao, and J. Suppe, 2000, 3-D restoration of complexly folded and faulted surfaces using multiple unfolding mechanisms: AAPG Bulletin, v. 84, p. 805–829.

Samson, P., 1996, Equilibrage de structures géologiques 3D dans le cadre du projet GOCAD: Thèse d'Ingénieur, Institut National Polytechnique de Lorraine, Lorraine, France, 222 p.

Sanders, C., M. Bonora, E. Kozlowski, and C. Sylwan, 2002, From 2D to 4D fracture network model, structural modeling of a complex thrust trap: A case study from the Tarija Basin, Argentina: Society of Petroleum Engineers, ISRM78184, p. 1–8.

Sanders, C., M. Bonora, D. Richards, E. Kozlowski, C. Sylwan, and M. Cohen, 2004, Kinematic structural restorations and discrete fracture modeling of a thrust trap: A case study from the Tarija Basin, Argentina: Marine and Petroleum Geology, v. 21, p. 845–855.

Sassi, W., S. E. Livera, and B. P. R. Caline, 1992, Quantification of the impact of sub-seismic scale faults on Cormorant block IV, *in* R. M. Larsen, H. Brekke, B. T. Larsen, and E. Talleraas, eds., Structural and tectonic modeling and its application to petroleum geology: Norwegian Petroleum Society (NPS), Special Publication, Elsevier, Amsterdam, v. 1, p. 355–364.

Schlische, R. W., S. S. Young, R. V. Ackermann, and A. Gupta, 1996, Geometry and scaling relations of a population of very small rift-related normal faults: Geology, v. 24, p. 683–686.

Shelton, J. W., 1984, Listric normal faults: An illustrated summary: AAPG Bulletin, v. 68, p. 801–815.

Walsh, J. J., and J. Watterson, 1991, Geometric and kinematic coherence and scale effects in normal fault systems, *in* A. M. Roberts, G. Yielding, and B. Freeman, eds., The geometry of normal faults: Geological Society (London) Special Publication 56, p. 193–203.

White, N. J., J. A. Jackson, and D. P. McKensie, 1986, The relationship between the geometry of normal faults and that of sedimentary layers in their hanging walls: Journal of Structural Geology, v. 8, p. 897–909.

Willemse, J. M., 1997, Segmented normal faults: Correspondence between three-dimensional mechanical models and field data: Journal of Geophysical Research, v. 102, p. 675–692.

Williams, G. D., and I. Vann, 1987, The geometry of listric normal faults and deformation in their hanging walls: Journal of Structural Geology, v. 9, p. 789–795.

Williams, G. D., S. J. Kane, T. S. Buddin, and A. J. Richards, 1997, Restoration and balance of complex folded and faulted rock volumes: Flexural flattening, jigsaw fitting and decompaction in three dimensions: Tectonophysics, v. 273, p. 203–218.

Withjack, M. O., Q. T. Islam, and P. R. La Pointe, 1995, Normal faults and their hanging-wall deformation: An experimental study: AAPG Bulletin, v. 79, p. 1–18.

Wriggers, P., 2002, Computational contact mechanics: New York, J. Wiley and Sons, 456 p.

Yamada, Y., and K. McClay, 2003, Application of geometric models to invert listric fault systems in sandbox experiments: Paper 1— 2D hanging wall deformation and section restoration: Journal of Structural Geology, v. 25, p. 1551–1560.

Yielding, G., J. J. Walsh, and J. Watterson, 1992, The prediction of small-scale faulting in reservoirs: First Break, v. 10, p. 449–460.